IEEE Access
Multidisciplinary ⋮ Rapid Review ⋮ Open Access Journal

Received June 16, 2021, accepted July 5, 2021, date of publication July 7, 2021, date of current version July 19, 2021.

Digital Object Identifier 10.1109/ACCESS.2021.3095422

A Review of Antenna Analysis Using Characteristic Modes

BASHAR BAHAA QAS ELIAS[1,2], (Member, IEEE), PING JACK SOH[1,3], (Senior Member, IEEE), AZREMI ABDULLAH AL-HADI[1], (Senior Member, IEEE), PRAYOOT AKKARAEKTHALIN[4,5], (Member, IEEE), AND GUY A. E. VANDENBOSCH[3], (Fellow, IEEE)

[1]Advanced Communication Engineering (ACE) CoE, Faculty of Electronic Engineering Technology, Universiti Malaysia Perlis (UniMAP), Pauh Putra Campus, Arau 02600, Perlis, Malaysia
[2]Department of Communication Engineering Techniques, Imam Ja'afar Al-Sadiq University, Baghdad 10052, Iraq
[3]Centre for Wireless Communications (CWC), University of Oulu, 90014 Oulu, Finland
[4]ESAT-WAVECORE Research Division, KU Leuven, 3001 Leuven, Belgium
[5]Department of Electrical and Computer Engineering, Faculty of Engineering, King Mongkut's University of Technology North Bangkok (KMUTNB), Bangkok 10800, Thailand

Corresponding authors: Bashar Bahaa Qas Elias (bashar.bahaa@sadiq.edu.iq) and Ping Jack Soh (pingjack.soh@oulu.fi)

This work was supported in part by the Ministry of Higher Education Malaysia through the Fundamental Research Grant Scheme under Grant FRGS/1/2020/TK0/UNIMAP/02/19, in part by the King Mongkut's University of Technology North Bangkok under Grant KMUTNB-FF-65-21, and in part by the Academy of Finland 6Genesis Flagship under Grant 318927.

ABSTRACT Characteristic modes can be used to solve many radiation and scattering problems involving fully conducting structures. The basic concept is to use eigenvalues and eigenvectors of the characteristic mode equations of a certain topology, and to use these eigenmode currents to control the radiating structure's behavior. This is accomplished by understanding the overall reflection and radiation characteristics across the operating frequency band. More specifically, characteristic modes are effective for example in determining the best location for the excitation of a radiating structure. In this paper, a comprehensive overview is provided to the different studies and their results obtained for different antennas that are based on the characteristic mode analysis method. A future perspective is given regarding the potential of this method in antenna analysis and design.

INDEX TERMS Antenna analysis, characteristic modes, antenna optimization.

I. INTRODUCTION

The theory of characteristic modes (TCM) was first proposed in [1] before being refined in [2], [3]. It is an efficient antenna design tool due to its capability in providing direct insights into the radiating phenomena on the antenna and allows the designer to design antennas more systematically in place of a brute force approach. These insights aid in the choice of excitation location on an antenna and on a platform [4]. This is to overcome the challenges of more complex antenna structures of today, where there is no closed formulation for their analyses.

Thus, the use of numeric methods [5], [6] becomes imperative. Therefore, the design of modern antennas relies on the use of numerical codes or commercial electromagnetic simulators such as IE3D, FEKO, Empire, or HFSS, among others, to simulate and predict the antenna performance before a physical protoType Is fabricated. Under these circumstances, the time required for the antenna design process is increased. Alternatively, characteristic modes analysis (CMA) enables the full attainment of the characteristics of a radiating body with arbitrary geometry with satisfactory level of computational accuracy. With clearer current distribution and radiation ability of each mode acquired from CMA, these radiating structures could be efficiently optimized. In addition to that, different feeding techniques can be applied to excite specific desired modes.

Characteristic modes are a representation of a set of orthogonal real currents on the surface of a conducting body. They depend only on the shape and size of the structure and are independent of the excitation [7]. Many different computational electromagnetic solvers have implemented different solvers to allow a more flexible way of designing antennas. However, CMA is unique as it does not require excitation

The associate editor coordinating the review of this manuscript and approving it for publication was Debdeep Sarkar.

sources when determining the electromagnetic properties of the structure. Thus, bandwidth of the structure can be better estimated more efficiently by solving only the equivalent eigenmodes. This produces a general electromagnetic solution for the structure, as the results of the analysis are independent of excitation [8]. Using a moment method formulation and the discretized impedance matrix, one can determine the characteristic modes of any perfectly conducting structure, and this feature is what make this method of analysis so attractive.

II. THE NEED FOR CMA

Most of antennas today are being designed using electromagnetic simulation software. The initial calculation of dimensions is performed before the structure is being modeled, excited and calculated in such software using methods such as Integral Equations (IE), which can be solved using Method of Moments (MoM) for complex environment with inhomogeneous lossy dielectrics, Finite Elements (FE), Finite Differences in the Time Domain (FDTD), and Finite Integration Technique (FIT). The calculation time is dependent on the complexity of the structure, details of the generated meshes, and the available computational resources. Thus, the procedure for optimizing the structure must be done systematically and efficiently.

In full-wave simulations, designers typically optimize a structure's parameters based on their understanding of its operating principles. Generated wave behaviors and performance parameters are the main guides to determining the next optimization steps for antennas, with the aid of these software. Such method can be suitable for simpler antenna topologies and becomes increasingly complicated as the antenna complexity increases with the combination of more operating principles into the same resonating structure at the same time.

Such software-based antenna design and optimization process can be made more systematic and efficient by generating and understanding the physical insights of the structure. This will then significantly reduce the required calculation time and effort, at the same time avoid the ''blind'' parameter adjustments within the optimization process. The use of the CMA enables the efficient tuning of an antenna to the correct resonant frequencies and determine the best locations to excite it. This is via the generation of the modes, modal significance, and surface current distributions. Auxiliary results such as the far field radiation patterns can also be used in the optimization process.

This paper reviews the state-of-the-art of the applied design and optimization process using CMA. They include different aspects of the optimization summarized in Table 1, aimed at making the processes more time- and resource-efficient.

The aim of this review paper is to review and discuss the recent progress in the topic of CMA. It is due to serve as an update of the state-of-the-art application of CMA, considering the previous most exhaustive reviews on this topic was performed more than five years ago in [4] and [9]. With the presentation of the recent developments, it is aimed at providing the latest information in understanding the applications and efficiency levels of CMA in the design process of

TABLE 1. Applied antenna design and optimization based on CMA from literature.

Category	Issue	Ref
Radiation Pattern Optimisation	Consistency of radiation patterns	[21]
	Optimization of radiation patterns	[22]
	Suppression of higher-order modes (HOMs) in multiport antennas	[23]
	Design of a null-steering antenna-based CMA	[24]
	Three dimensional null-scanning antennas using TCM	[25]
	Improving radiation efficiency of a mounted-on-platform radiator based on CMA	[26]
	Suppress cross polarization using CM analysis	[20]
Feed Optimisation	Optimization of feeding structure	[27]
	Resonant behavior optimization of different antenna excitations	[28]
	Finding the optimal feeding point of the antenna using CMA	[20]
Impedance Matching Optimisation	Identify the impedance mismatch of the antenna	[29]
	Achieving Ultrawideband (UWB) performance for antennas	[30]
	Design of wideband wearable antenna using CMA with the ground as a part of the radiator	[31]
	Optimization of a nonuniform metasurface	[32]
	Design of bandwidth-enhanced and multiband multiple-input–multiple-output (MIMO) antennas	[33]
	Bandwidth enhancement of platform-mounted high frequency (HF) antennas.	[34]
	Three empirical techniques using CMA to achieve a wideband design	[35]
MIMO	Ultra-wideband multi element antenna for massive MIMO indoor base stations	[36]
	Systematic design of a multiport MIMO antenna with bilateral symmetry	[37]
Space Applications	Design antenna for nanosatellite applications	[38]
	Guideline for enabling the hosting platform as part of the radiating system	[39]
Metasurface	Substrate-integrated gap waveguide (SIGW)-fed metasurface antenna array with nonuniform excitation	[40]
	Wideband metasurface antennas	[41]
	Dual-wideband dual-polarized antenna using metasurface for 5G millimeter wave communications	[42]
	Resonant metasurface antennas with resonant apertures	[43]
Platform	Exploiting the metallic platform as the main radiator using CMA.	[44]
	Design platform embedded HF antennas based on CMA	[45]
	Design for an electrically small unmanned aerial vehicle based on characteristic modes.	[46]
Tracking of Modes	Modes tracking and sorting	[47-49]
	Design guidelines by manipulating the coupling of modes	[50]
	Reducing the design optimization time	[51]
	Addiiton of a lower band and improvement of isolation	[52]

antennas and passive components. The rest of the manuscript is organized as follows. The next section presents the operating principle of the characteristic mode analysis method. Section IV details a survey of the different applications and impacts of using CMA in the design and optimization processes for different antenna types. A summary and the future perspectives presented in Section V concludes this review.

III. THEORY OF CHARACTERISTIC MODE

Harrington and Mautz in [2] considered the problem of using one or more conducting bodies, which is defined by the surface S, in an impressed electric field E^i. An operator equation for the current J on S was expressed as:

$$[L(J) - E^i]_{\tan} = 0 \tag{1}$$

where the subscript "tan" denotes the tangential components on S.

Harrington then improved this by proposing a simpler derivation. A modal solution for the current J on a conducting body is obtained by using the eigencurrents as both expansion and testing functions in the Method of moment (MoM). By adhering to the procedures in [2], J has been assumed to be a linear superposition of the mode currents. Besides that, the electric and magnetic fields are linearly related to the currents, and hence, can also be expressed in modal forms.

In a general antenna analysis technique based on MoM, two important conditions must be known: the structure of the antenna and its excitation or incident field. Meanwhile, in CMA, only the structure of the antenna is required as a known condition. The characteristic modes are obtained by solving the following mathematical equations [2]:

$$\vec{J} = \sum_n a_n J_n \tag{2}$$

where J_n is the eigencurrent and a_n is the modal weighting coefficient.

$$a_n = \frac{V_n^i}{1 + j\lambda_n} \tag{3}$$

where λ_n is the eigenvalue and V_n^i is the modal excitation coefficient. The modal significance, MS_n, which is represented by the normalized amplitude of the current modes is calculated as follows [2]:

$$MS_n = \left| \frac{1}{1 + j\lambda_n} \right| \tag{4}$$

The modal significance is ranged between $0 < \text{MS} \leq 1$. Identically, a mode is at resonance when its associated model significance, MS is unity (equals to 1). On the other hand, the characteristic angle (β_n), can be calculated as follows [10]:

$$\beta_n = 180 - \tan^{-1}(\lambda_n) \tag{5}$$

These three important coefficients of the CMA are summarized in Table 2.

It is observed that when the characteristic angle is within 90° or 270°, the mode mainly stores energy. In addition to this, the value of the characteristic angle indicates whether the mode contributes to storing magnetic energy in an inductance mode (when $90° < a_n < 180°$) or storing electric energy in a capacitance mode (when $180° < a_n < 270°$).

TABLE 2. Summary of the three coefficients of the characteristic mode.

Eigenvalue λ_n	Model Significance MS	Characteristic Angle (β_n)	Mode Status
$\lambda_n > 0$	0<MS<1	$90° < \beta_n < 180°$	Inductive
0	1	180°	Resonant
$\lambda_n < 0$	0<MS<1	$180° < \beta_n < 270°$	Capacitive

IV. DESIGN AND OPTIMIZATION APPLICATIONS

To illustrate how CMA is applied in facilitating the design and optimization process of the different antenna types, several examples are reviewed in detail. They include the widening of the impedance bandwidth of planar, wire antennas [11]–[14], and multiport antennas for MIMO systems [13], [15]–[19]. More details of the theoretical and practical developments of CM-based methodologies for a variety of antenna designs have been presented in [20], with selected ones also included in this paper. The main objectives of the use of CMA, parameters optimized in the literatures, and software used in CMA simulations are summarized in Table 3. They will be explained further in the following sections.

A. RADIATION PATTERN OPTIMISATION

This section focuses on presenting the application of the CMA technique in optimizing the radiation pattern of the antennas. The available literature includes examining the polarization and avoiding the distortion of the radiation pattern based on the response of the CMA parameters such as current distribution and the modal significance. They are explained as follows.

A simple dipole and a loop antenna structure are designed and optimized based on the theory of characteristic modes in [21], as illustrated in Fig. 1. The modal weighting coefficients of non-resonant modes of the proposed antenna are always far smaller compared to resonant modes, indicating the significance of the modes. To determine the best feeding location, three cases will be discussed, i.e., when the antenna is fed at point A, point B, and point C, as shown in Fig. 2.

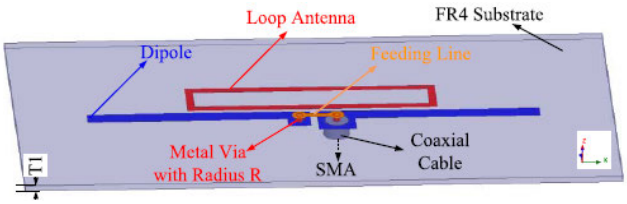

FIGURE 1. Loop antenna geometry [21].

The aim is to widen the impedance mode bandwidth of each structure. It is achieved by simultaneously exciting the

TABLE 3. An overview of different antennas based on CMA from literature.

Ref	Work	Frequency band	Substrate and size information, parameters optimized	Software used
[21]	Wideband Antenna with Stable Omnidirectional Radiation Pattern	S-band (1.85 to 2.9) GHz	Substrate: FR4, ε_r = 4.4, $tan\delta$ =0.02, thickness = 0.8 mm Loop antenna size = 22×6×1 mm^3 Dipole antenna size = 66×2 mm^2 Substrate size = 80×40×0.8 mm^3 A new wideband antenna with stable omnidirectional radiation pattern is investigated based on CMA	FEKO
[29]	Bandwidth Enhancement of Circular Microstrip Antenna	S-band (2.40 to 2.48) GHz	Substrate: FR4, ε_r = 4.3, $tan\delta$ =0.02, thickness = 0.16 mm Circular part radius = 17.3 mm Slot length and width = 12 and 1 mm Ground plane size = 44×59 mm^2 Substrate thickness = 1.6 mm CMA used to identify possible causes of impedance mismatches for a circular microstrip antenna	CST MWS
[27]	Compact Low-profile UWB Antenna for UHF TV White Space Devices	UHF (474 to 1212) MHz	Substrate: FR4, ε_r = 4.4, $tan\delta$ =0.02, thickness = 0.8 mm Rectangular plate size = 145×35×0.8 mm^3 CMA guided the feeding structure design and parameter optimizations	FEKO
[30]	An UHF UWB Doubled Annular Ring Antenna	UHF (470 to 960) MHz	Substrate: Rogers 5880, ε_r = 2.2, $tan\delta$ =0.0004, thickness = 3.1 Radius R01=32, R02=22, R11=53, R12=30, R21=73, R22=50, R31=100, R32=70 mm CMA used to design and optimize the antenna structure	FEKO
[22]	Design of Wideband Omnidirectional Antenna	C-band (5.06 to 6.18) GHz	Substrate with ε_r = 4.4, $tan\delta$ =0.02, thickness 1 = 3 mm, thickness 2 = 0.8 mm 38.2×8.8 mm^2 TCM used to realize horizontally polarized omnidirectional radiation patterns	CST MWS
[23]	A Method of Suppressing Higher-Order Modes for Improving Radiation Performance of Metasurface Multiport Antennas	C-band (4.9 to 5.9) GHz	Substrate 1 and 2: Rogers RO4003C, ε_r = 3.55, $tan\delta$ =0.0027, thickness of substrate 1 = 0.508 mm, thickness of substrate 2 = 3.048 mm Radius of ring = 8.5 mm Width of ring = 0.4 mm Length of the dipole = 19.5 mm Substrate thickness = 0.508 mm CMA used to suppress the unwanted HOMs of the metasurfaces in multiport antenna systems to improve the radiation performance	FEKO
[24]	Null-Steering Antenna Design by using Phase Shifted Characteristic Modes	S-band (2.37 to 2.47 GHz)	Substrate: FR4, ε_r = 4.4, $tan\delta$ =0.02 thickness = 1.2 mm Overall antenna dimensions: 150 x 150 mm^2 and 154 x 154 mm^2 Radiation pattern is optimized.	Not reported
[25]	Advantageous Exploitation of Characteristic Modes Analysis for the Design of Three-Dimensional Null Scanning Antennas	S-band (2.4 to 2.5 GHz)	Substrate: Single-sided FR4, ε_r = 4.4, $tan\delta$ =0.02, thickness = 1.2 mm. Conductive capacitive exciters are printed on the FR4. A new strategy for placing a null of the pattern of a reconfigurable antenna in any desired direction is proposed.	Not reported
[26]	Efficient Excitation of Characteristic Modes for Radiation Pattern Control by Using a Novel Balanced Inductive Coupling Element	CMs of the rectangular box are calculated from 60 to 70 MHz	Mounted-on-platform radiator, rect box: L = 3.4 m, W = 2 m, and D = 1 m. A design strategy-based CMA described for improving the radiation efficiency of a mounted-on-platform radiator.	FEKO
[51]	Characteristic Mode Analysis of Microstrip Patch Shapes	S-band and C-band (between 2.5 and 8.5) GHz	Circular patch radius = 9.71 mm Square patch = 17.21 mm Elliptical patch radius = 6 and 15.71 mm Parallelogram base = 20.25 mm Regular pentagon side = 13.12 mm Regular octagon side = 7.83 mm CMA used to analyze the resonant behaviors of different patch shapes	FEKO
[28]	Characteristic Mode Analysis of Excitation Feed Probes in Microstrip Patch Antennas	S-band and C-band 2.5 to 5.7 GHz (conventional probe) 2.5 to 6.1 GHz (L- probe) 2.5 to 7.0 GHz (T- probe)	Substrate with ε_r = 4.4, $tan\delta$ =0.02 CMA used to optimize the antenna structure with towards broadband behavior	FEKO
[31]	Design of Wideband Wearable Antenna using Characteristic Mode Analysis	S-band (2.05 to 2.7) GHz Estimated from the figure	Substrate 1: FR4, ε_r = 4.3, $tan\delta$ = 0.044, thickness = 1.6 mm Substrate 2: Felt, ε_r = 1.3, $tan\delta$ = 0.044, thickness = 3 mm Substrate diameter: 15mm Patch diameter: 13 mm CMA used to analyze the characteristic modes of the ground, and choosing the suitable location of the button on the ground	CST MWS
[50]	A Vertically Polarized Patch Antenna with Switchable Near-Endfire Beam	S-band (2.145 to 2.227) GHz	Substrate: Rogers RT/duroid 5880, ε_r = 2.2, thickness = 1.575 mm Antenna size = 300 × 100 mm^2 (2.17 λ_o × 0.72 λ_o) Three square patches with 30 × 30 mm^2 each (0.217 λ_o × 0.217 λ_o) CMA guided to the best choices of modes and optimal coupling from perspectives of gain and sidelobe level	CST MWS
[20]	U-slot Microstrip Antenna E-slot Microstrip Antenna	S-band (2.2 to 2.7 GHz) S-band (2.35 to 2.55), as estimated from the figure.	Substrate: FR4, ε_r = 4.4, $tan\delta$ = 0.02, thickness = 1.6 A foam with dielectric constant of εr = 1.1 is used to support the E-shaped patch The radiating patch was fabricated using 0.5 mm thick copper sheet CMA used to analyze the radiating patch	HFSS
[52]	LTE Band Integrated 5G Antenna Design	L-band (0.69 to 1.19 GHz) S-band (2.29 to 3.29 GHz) (3.93 to 4.6 GHz) C-band (5.52 to 6.45 GHz)	Substrate: RT-Duroid, ε_r = 3.2, $tan\delta$ = 0.0009, thickness = 0.762 mm Dimension of the individual patches: 12 × 4 mm^2 CMA used to design the lower band operation.	CST MWS
[32]	Characteristic Mode Analysis of a Nonuniform Metasurface Antenna for Wearable Applications	S-band (2.05 to 2.7 GHz) Estimated from the paper	Substrate 1: FR4, ε_r = 4.3, $tan\delta$ = 0.044, thickness = 1.6 mm Substrate 2: Felt, ε_r = 1.3, $tan\delta$ = 0.044, thickness = 3mm Substrate diameter = 15mm Patch diameter = 13 mm CMA used to optimize the operating band of the antenna by combining characteristic modes	CST MWS
[33]	Design of Bandwidth-Enhanced and Multiband MIMO Antennas Using Characteristic Modes	LTE (dual-band): (818 to 896 MHz) (1841–2067 MHz)	Substrate: polycarbonate material, ε_r = 2.27, $tan\delta$ =0.012, thickness = 8 mm Total dimensions of 130 × 66 × 8 mm^3 chassis and a 20-mm rotationally symmetric capacitive loading offset. TCM used to enhance the performance of the orthogonal MIMO antennas	CST MWS
[34]	Bandwidth Enhancement of Platform-Mounted HF Antennas Using the Characteristic Mode Theory	HF band (3 to30 MHz)	Substrate: Rogers RT/duroid 5880, ε_r = 2.2, thickness = 0.508 mm. A simple metallic platform in the shape of a rectangular box with dimensions of 3.7 m × 10.7 m × 3.3 m. Examined how the characteristic modes of the platform can be excited using CMA to increase the overall bandwidth	FEKO
[35]	Characteristic Mode Analysis of a Class of Empirical Design Techniques for Probe-Fed, U-Slot Microstrip Patch Antennas	L and S-bands 1 to 4 GHz	Substrate: FR4, ε_r = 4.4, $tan\delta$ =0.02, thickness = 11.811 mm Finite, grounded dielectric substrate. CMA used to determine critical parameters such as substrate electrical thickness, slot width, probe radius and feed location variations.	FEKO
[36]	Compact Multi Mode Multi Element Antenna for Indoor UWB Massive MIMO	C-band 6 GHz to 8.5 GHz.	Substrate: Rogers RO4003C, ε_r = 3.55, $tan\delta$ =0.0027, thickness = 813 µm Overall Multi-Mode Multi Element Antenna (M^{3}EA) dimension: approx. 70 cm × 70 cm (1.69 λ_o × 1.69 λ_o) The outer dimensions of the final element (0.85 λ_o × 0.85 λ_o). When using crossed dipoles, the size of an element (0.5 λ_o × 0.5 λ_o) Center frequency fc = 7.25 GHz Proposed a new concept for compact multi-element antennas based on the CMA approach.	Not reported

TABLE 3. ***(Continued.)*** **An overview of different antennas based on CMA from literature.**

[37]	Systematic Design of a Multiport MIMO Antenna with Bilateral Symmetry Based on Characteristic Mode Analysis	S-band (2.4 GHz ISM band)	Substrate: FR4, ε_r = 4.3, $tan\delta$ =0.025, thickness = 0.5 mm. The dimensions of the bug-like conducting body is 50 mm × 61.5 mm × 10 mm (0.4λ_o × 0.49λ_o × 0.08λ_o at 2.4 GHz). A multiport MIMO antenna is designed and optimized using CMA.	CST MWS and FEKO
[38]	Characteristic Modes Analysis of Non-Uniform Metasurface Superstrate for Nanosatellite Antenna Design	S-band (2.025 – 2.29 GHz).	Substrate: Rogers TMM3, ε_r = 3.46, $tan\delta$ =0.002, thickness = 6.985 mm Metasurface (MTS) antenna of (0.068 λ_o). Non-uniform MTS based on rectangular patches are optimized.	HFSS and CST MWS
[39]	A Compact CubeSat Antenna with Beamsteering Capability and Polarization Agility	S-band (2.4 – 2.45 GHz).	Substrate: RO5880, ε_r = 2.28, $tan\delta$ =0.0009, thickness = 0.254 mm A 1 U CubeSat mockup (dimensions 10 cm × 10 cm × 10 cm). The non-resonant balanced inductive exciter (BIEs) are placed on the top face of the cube. Each half loop is 5 mm in height and 10 mm in length CubeSat is designed and optimized based CMA.	FEKO
[40]	Wideband Sidelobe-Level Reduced Ka-Band Metasurface Antenna Array Fed by Substrate-Integrated Gap Waveguide Using Characteristic Mode Analysis	Ka-band (27.7–40 GHz)	Substrate: Rogers RT5880, ε_r = 2.2, thickness = 0.787 mm. A single-layered 2 × 2 patch-based metasurface. The CMA has been successfully employed for metasurface synthesis and feeding placement. The antenna dimensions and reflection coefficient are optimized.	CST MWS
[41]	Low-Profile Wideband Metasurface Antennas Using Characteristic Mode Analysis	C-band (4.85 to 6.21 GHz)	Substrate: Rogers RO4003C, ε_r = 3.55, $tan\delta$ =0.0027, thickness = 3.454 mm and 0.508 for patch-ground layer and ground-feed layer, respectively. Overall size of 1.78λ_o×1.78λ_o×0.07λ_o. The CMA is used for the modeling, analysis, and optimization of the proposed antenna to reveal the underlying modal behaviors of the metasurface and to guide the mode excitation.	CST MWS
[42]	Dual-Wideband Dual-Polarized Metasurface Antenna Array for the 5G Millimeter Wave Communications Based on Characteristic Mode Theory	K and Ka-bands (24.2-27.8 GHz) (BW = 13.85 %) (36.9-42.8 GHz) (BW = 4.81 %)	Substrate: Rogers RT5880, ε_r = 2.2, $tan\delta$ = 0.0009, thickness = 0.787 mm. Metasurface is composed of a 3×3 quasi square patch. Dual-polarized metasurface antenna array is optimized based on CMA.	CST MWS
[43]	Resonant Metasurface Antennas with Resonant Apertures: Characteristic Mode Analysis and Dual-Polarized Broadband Low-Profile Design	C-band (4.8–6.2 GHz)	Substrate with ε_r = 2.2, $tan\delta$ =0.0009, thickness = 3.14 mm and 0.508 mm for Substrates I and II, respectively Overall size of λ_L×λ_L×0.058λ_L (λ_L is the free-space wavelength at 4.8 GHz). Four-step CMA framework is formulated for gaining physical insights into the operating principle of the resonant metasurface (MTS) antennas.	FEKO
[44]	Design of Dual-Polarized, Platform-Based HF Antennas Using the Characteristic Mode Theory	HF band (3 to 10 MHz).	Earth type: Dry (ε_r = 3), Wet earth (ε_r = 30), Sea water (ε_r = 30) The size of elements 1 and 2 is 0.006 λ_o × 0.042 λ_o × 0.008 λ_o (0.6 × 4.2 × 0.8 m^3) and the size of element 3 is 0.02 λ_o × 0.03 λ_o × 0.006 λ_o (2 × 3 × 0.6 m^3) at 3 MHz TCM is used to exploit the metallic platform as the main radiator to overcome the bandwidth and efficiency limitations of electrically antennas.	FEKO
[45]	HF Band Shipboard Antenna Design Using Characteristic Modes	HF band (3 to 30 MHz)	Dimensions of the naval ship = 204 × 30 m^2 (3.4 λ_o × 0.5 λ_o) at 5 MHz. The CMs are first solved to understand the resonant behavior of the ship platform. Second, the radiating currents are synthesized to produce designated radiation patterns using the CMs of the ship platform.	HFSS
[46]	Electrically Small UAV Antenna Design Using Characteristic Modes	UHF-band (785 to 815 MHz), as estimated from the figure.	Substrate: FR4, ε_r = 4.4, $tan\delta$ =0.02, thickness = 1.6 mm, with a size of 80 × 10 mm^2 (0.218 λ_o × 0.027 λ_o). Center frequency of fc = 820 MHz. F-shaped probe is used to excite the platform current. The electrical size of the small UAV is 0.648 λ_o × 0.746 λ_o × 0.154 λ_o. Multi-objective evolutionary algorithm is implemented to synthesize currents on the body to achive desired power patterns based on theory of CM.	HFSS

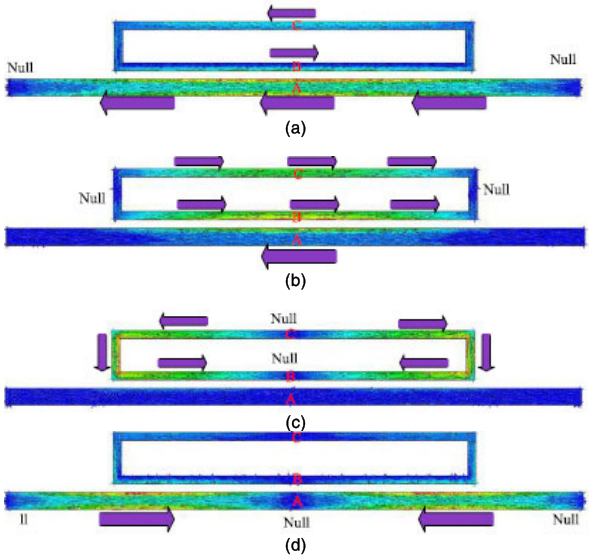

FIGURE 2. **Current distributions of (a) mode 1 at 2 GHz, (b) mode 2 at 3.05 GHz, (c) mode 3 at 3.25 GHz, and (d) mode 4 at 4.1 GHz of the proposed antenna [21].**

antenna's first two modes, which are closely spaced between each other, as follows:

i. *Case 1:* When fed at point A, both mode 1 and mode 2 are strongly excited, especially around their resonant frequencies.
ii. *Case 2:* When fed at point B, mode 2 is well excited but mode 1 is not excited equivalently even at its resonant frequency.
iii. *Case 3:* When fed at point C, mode 2 is well excited but mode 1 is not excited equivalently even at its resonant frequency.

In this study, only significant modes with characteristic angles of close to 180° have been considered. Hence, it can be observed that point A is the best feeding location, as shown in Fig. 3. Besides a similar omnidirectional radiation pattern produced by these two modes, a consistent radiation pattern is also achieved throughout the operating frequency band, as shown in Fig. 4.

Next, three antennas have been proposed to produce horizontally polarized omnidirectional radiation patterns for the fifth generation (5G) and wireless local area network (WLAN) communication. Their structures are depicted in Fig. 5, indicated as type I, type II, and type III. Type I is a conventional microstrip square patch, whereas type II and Type III are based on the modifications of the type I structure. CMA is used to facilitate the analysis of these structures [22]. It is observed that between the 5 and 6 GHz range, several MSs are greater than 0.7, as shown in Fig. 6. It indicates that these modes can be effectively excited. For the Type I and II structures, the excited modes are narrower in bandwidth compared to the modes of Type III.

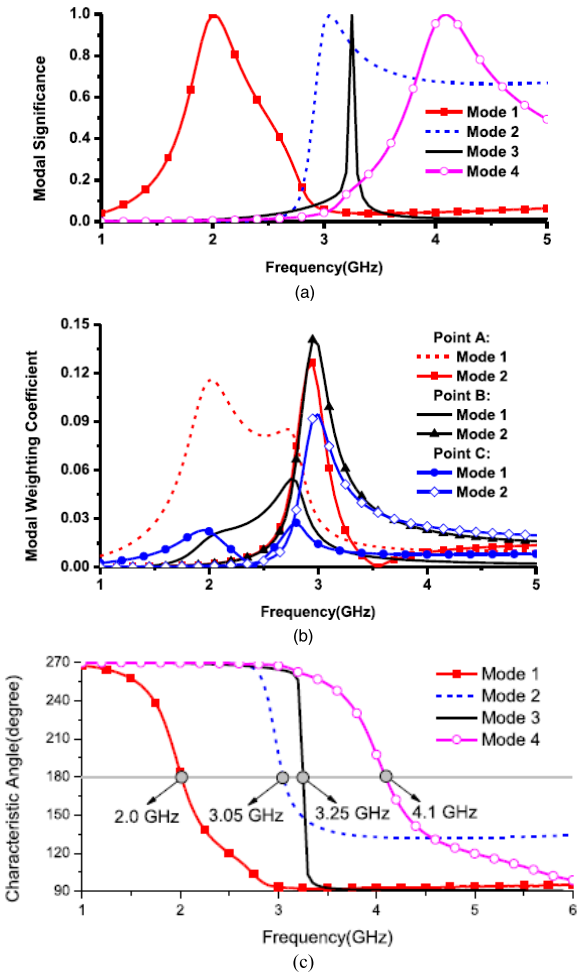

FIGURE 3. (a) Modal significance for the first four modes of the antenna in [21] (b) Modal weighting coefficients for the first two modes of the same antenna with different feeding locations [21] (c) Characteristic angles of the first four modes [21].

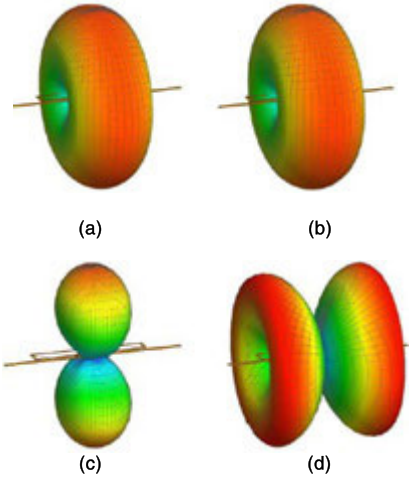

FIGURE 4. Radiation patterns of (a) mode 1 at 2 GHz, (b) mode 2 at 3.05 GHz, (c) mode 3 at 3.25 GHz, and (d) mode 4 at 4.1 GHz of the proposed antenna [21].

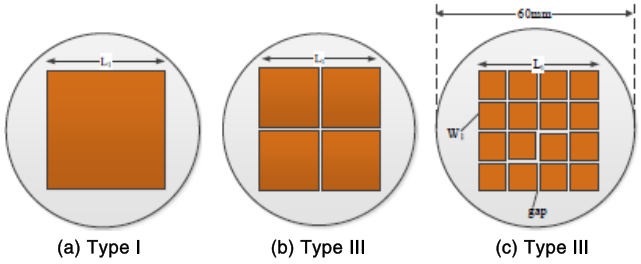

FIGURE 5. Simulated VSWR of the proposed antenna [22].

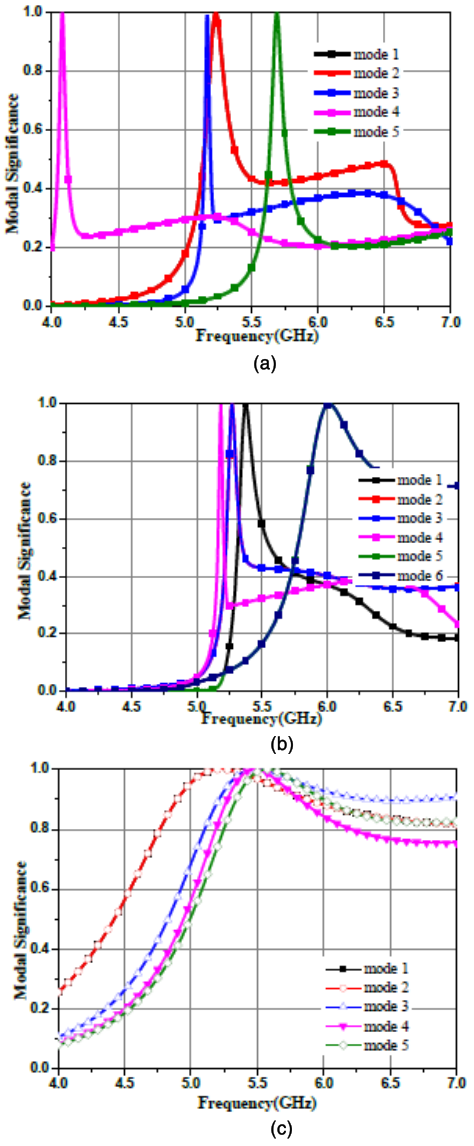

FIGURE 6. Modal significance of the three structures (a): Type I (b): Type II (c): Type III [22].

It should be noted that from Fig. 7(a), the modal radiation pattern for structure Type II (of mode 1) is omnidirectional. On the other hand, the modal radiation pattern in Fig. 7(b) also resulted in an omnidirectional radiation pattern.

Meanwhile, a four-port antenna system with metasurfaces comprising of square patches is presented in the study shown

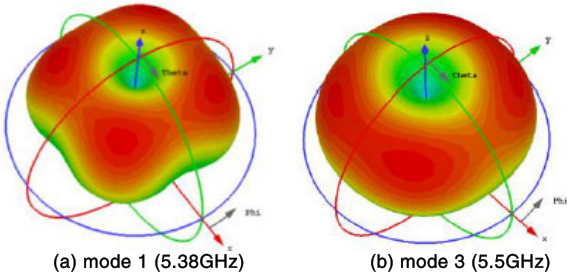

FIGURE 7. The modal radiation patterns for structure Type II and III at the respective resonant frequencies [22].

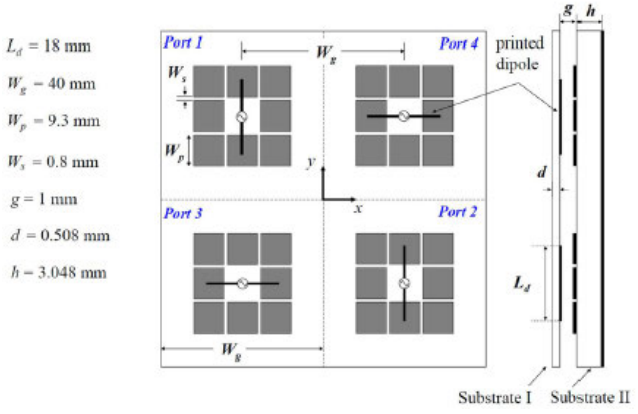

FIGURE 8. Configuration of the four metasurface antennas [23].

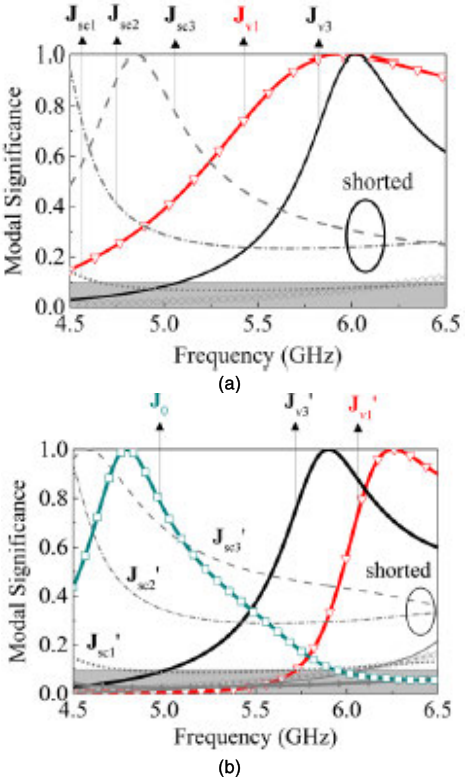

FIGURE 9. Modal significance of the slot-via loaded metasurface (a) without dipole (b) with dipole [23].

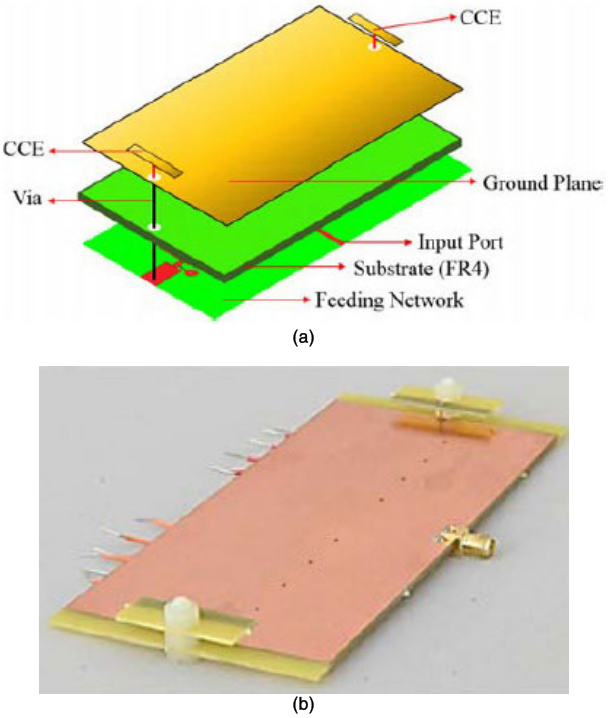

FIGURE 10. Geometry of the antenna (a): simulation prototype (b): measurement prototype [24].

in Fig. 8 [23]. The modal currents are controlled by loading the unit cells of the metasurface with slots and vias for the suppression of the higher-order modes (HOMs). These modal currents are also optimised in addition to their resonance frequencies by observing the modes of the metasurface. This is done by suppressing the unwanted HOMs in the metasurfaces to avoid radiation pattern distortion. Suppression is done in this work by adding slots and ground into the unit cells of the metasurface. From Fig. 9, it is noticed that three new modes resonating below 5 GHz are introduced, denoted as J_{sc}, where the subscript indicates the ''short-circuit'' condition.

In [24], the CMA method is used to determine the most promising current modes which can contribute to form the desired pattern. The structure of the proposed antenna in this study is illustrated in Fig. 10. Firstly, the CM analysis on the conducting plane, which is modeled based on a handheld device dimensioned at 150×75 mm^2. This is done to find the proper position of the capacitive coupling elements (CCEs) used to excite the relevant current modes at 2.45 GHz. The MS of the first eight modes of the proposed antenna is shown in Fig. 11. It is observed that in the frequency range of interest, most of the modes have a value near to one, except for mode 5 and mode 6. It is found that only modes 4 and 8 are relevant to be excited, as shown in Fig. 12(a)-(b). Mode 4 produces a pattern with a null in the broadside direction ($\theta = 0°$), whereas mode 8 produces a pattern with nulls near $\theta = \pm 30°$ (see Fig. 12(c)-(d)).

Another study in [25] presented the design strategy for realizing three dimensional null-scanning antennas by using CMA. This is performed by exploiting the variation of the

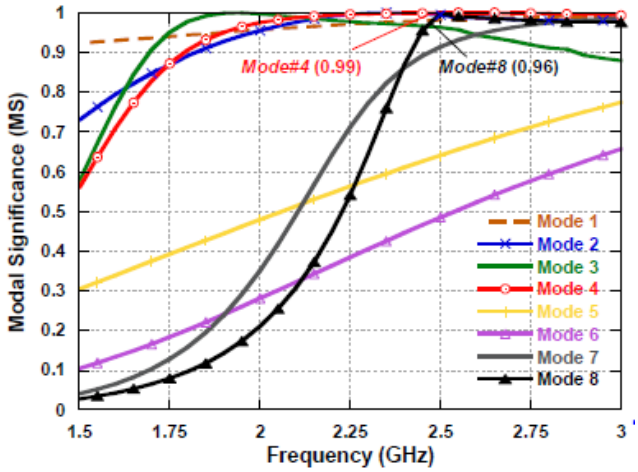

FIGURE 11. MS of the antenna with CCEs [24].

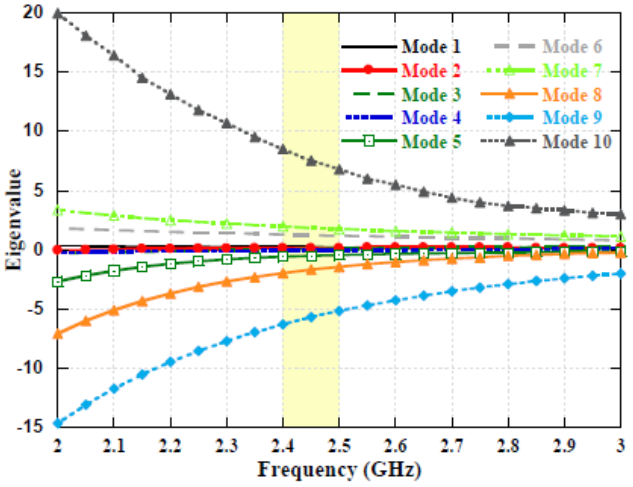

FIGURE 13. Eigenvalues as a function of frequency [25].

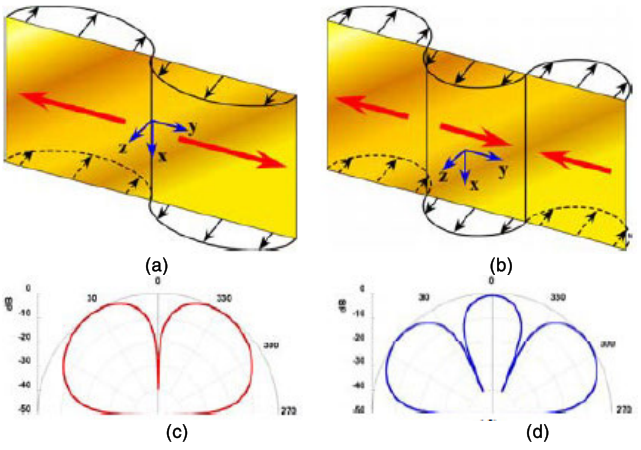

FIGURE 12. Analysis of the currents and patterns at 2.45 GHz in selecting the desired current mode: (a): mode 4 (b): mode 8 and radiation pattern produced by (c): mode 4 and (d): mode 8 [24].

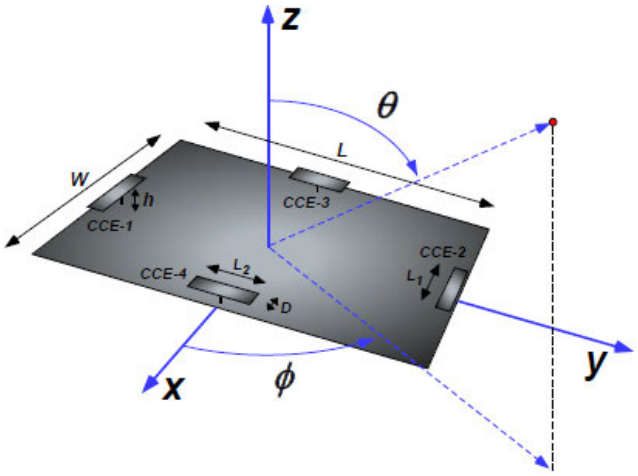

FIGURE 14. Rectangular conductive plane with four capacitive exciters; $L = 150$ mm, $W = 75$ mm, $L1 = 33$ mm, $L2 = 35$ mm, $D = 5$ mm. [25].

excitation degree of the current modes (Jn) over the investigated platform. By doing so, a null in the pattern can be placed in any desired direction in the upper hemisphere. First, the CMA of the rectangular conductive plane is performed.

This resulted in a set of orthogonal current modes (Jn) distribution that depends only on the antenna geometry, independent of any external excitation. The eigenvalues (λn) for the first ten modes of this rectangular plane are shown in Fig. 13. This parameter determines the reactive power related to each mode. These eigenvalues are real numbers and a mode is considered resonant when its associated value is equal to zero. A particular mode is easier to excite and contributes more significantly to the total radiated power with close-to-zero eigenvalues. It is apparent that in the frequency range of interest (from 2.4 to 2.5 GHz), most of the modes have an eigenvalue magnitude lower than 2, except for mode 7, 9 and 10, which are higher order modes. Specifically, mode 7 and 10 are identified as inductive modes ($\lambda > 0$), whereas mode 9 is a capacitive mode ($\lambda < 0$). Therefore, these higher order modes do not significantly contribute to the total radiated power in this frequency range. Four capacitive exciters have been used with the rectangular conductive plane as shown in Fig. 14.

Next, the normalized modal weighing coefficient (MWC) amplitude analysis is performed when the CCEs are individually excited. This helps to understand which current modes are efficiently excited over the conductive plane within 2.4 to 2.5 GHz. Fig. 15 shows that the sources located along the y-axis (Port 1 and Port 2) can excite both modes 2 and 8 from the antenna. On the contrary, the CCEs located along the x-axis (Port 3 and Port 4) allows the efficient excitation of modes 2 and 5. The prototype of the proposed null-scanning antenna is illustrated in Fig. 16.

Another work in [26] presented the improvement of the radiation efficiency of a mounted-on-platform radiator using a Balanced Inductive Exciter (BIE). This is introduced to improve the modal excitation purity of selected CMs. The MS of the first five modes within the 50 to 80 MHz bandwidth

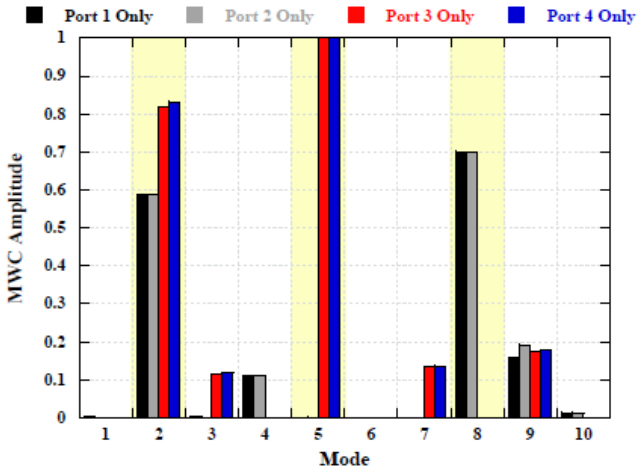

FIGURE 15. Normalized amplitude of the MWC when the CCEs are individually excited at 2.45 GHz [25].

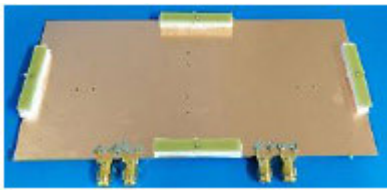

FIGURE 16. Radiating element with the four CCEs [25].

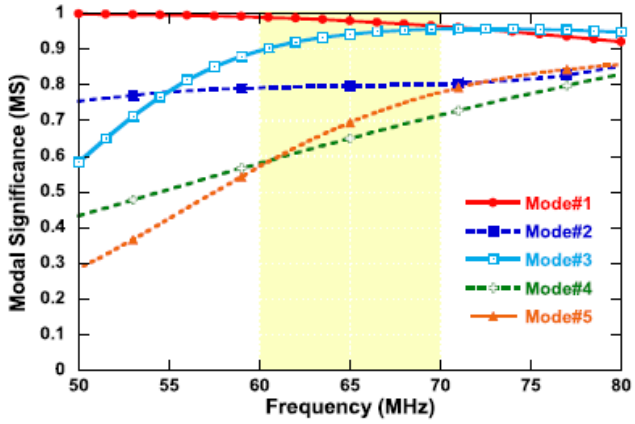

FIGURE 17. MS of the first five characteristic modes as a function of the frequency [26].

is shown in Fig. 17 for a rectangular box. For this structure, the first five modes produced near-to-unity MS. This parameter indicates the resonant modes (with MS = 1), and therefore largely contributes to the total radiated power (*Pr*) in a particular frequency range.

The new BIE excitation proposed in this study, in contrast to the commonly adopted Unbalanced Inductive Exciter (UIE) excites the current distribution on the platform, as shown in Fig. 18(a) and (b). A rectangular box with inductive coupling exciter (ICEs) placed on the top face are compared for both the UIEs and BIEs configuration. From the

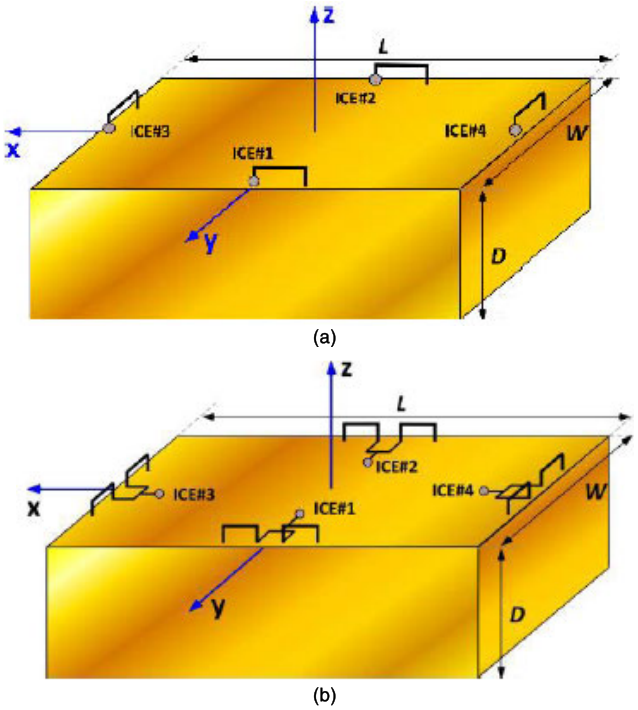

FIGURE 18. ICEs arrangement over a rectangular box. (a) conventional UIE configuration. (b) proposed BIEs configuration [26].

preliminary analysis, the excitation arrangement of the proposed BIEs allows a better modal selective excitation than the unbalanced feed configuration from the UIE configuration. Thus, a better excitation purity of the first four modes can be obtained by properly controlling their amplitudes and phases. A comparison of the normalized MWC amplitude between the UIEs and BIEs configuration on the box is illustrated in Fig. 19.

Another study in [20] presents a CM analysis method to detect circular polarization and cross polarization on a radiating patch. The prototype of the analyzed non-symmetrical E-shaped patch antenna is shown in Fig. 20, which is chosen due to its capability to widen impedance bandwidth. Fig. 21 shows the variations in characteristic angle and modal significance with frequency for the first three modes. As can be observed, modes 1 and 2 showed the same modal current magnitudes at 2.3 GHz, whereas modes 2 and 3 produced the same current magnitudes at 2.6 GHz. In addition to that, the physical interpretations of the CMs indicated that mode 3 and all other higher order modes contribute insignificantly to the radiated energy at 2.3 GHz. This is due to their low associated modal significance (<1), which indicates the difficulty in exciting them. Fig. 21 indicates that modes 1 and 2 can potentially be combined for CP near 2.3 GHz, and modes 2 and 3 can also be combined to generate CP near 2.6 GHz due to their equal modal amplitudes. However, since mode 1 is the dominant mode at 2.6 GHz, CP may be more difficult to be generated due to the higher potential of

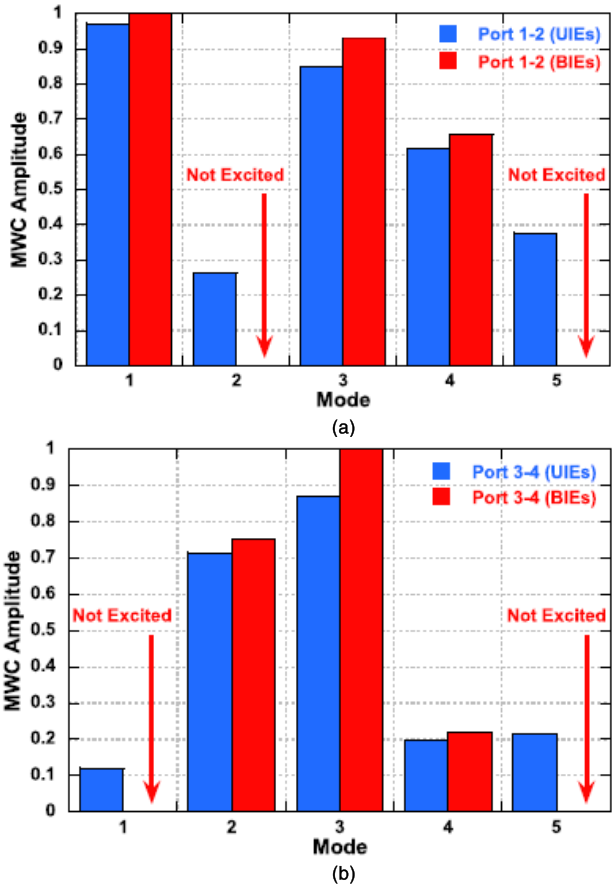

FIGURE 19. Comparison of the normalized MWC amplitude between the UIEs and BIEs configuration on the box (a): Ports 1 and 2 (b): Ports 3 and 4 [26].

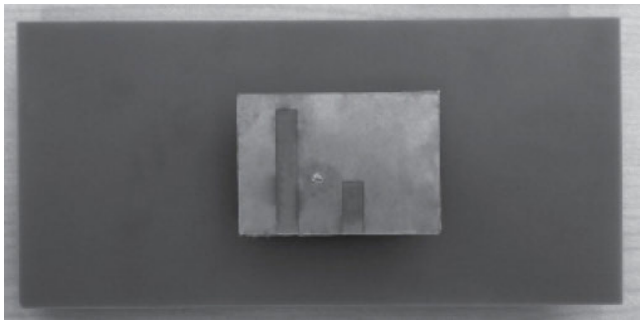

FIGURE 20. The geometry of the circularly polarized (CP) E-shaped patch antenna [20].

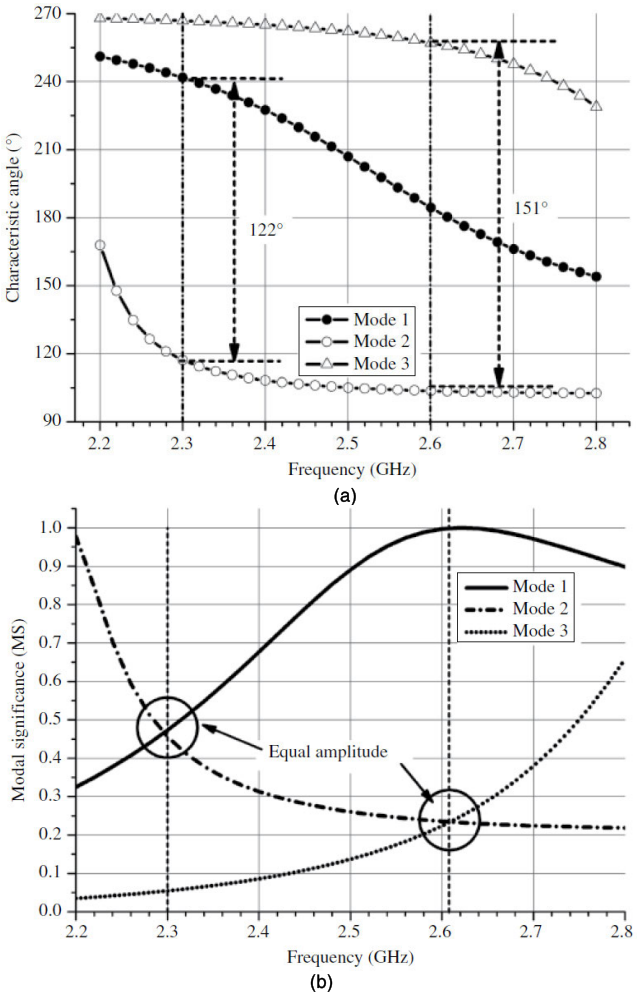

FIGURE 21. The first three characteristic modes of the E-shaped patch antenna (a): characteristic angle and (b): modal significance [20].

cross-polarization level generation. Thus, the CP is chosen to be generated at 2.3 GHz instead.

B. FEED OPTIMISATION

This section presents methods in applying the CMA approach for antenna feed optimization. Feed structure can be optimized efficiently to obtain the best response of the antenna around the desired frequency. In addition, this method can be applied in finding the optimal position to excite the antenna by studying the current distribution on the antenna surface for the dominant modes. These methods are explained as follows.

It is well known that the ground, and the substrate structures will not significantly affect the distribution of eigen currents on the radiating plane. Despite that, changes in these components are expected to affect the modal resonances. Modes become complex after the ground, feeding strip and substrate are incorporated. This concept is demonstrated using a planar dipole antenna in [27]. The current distributions for the five significant modes of the dipole are depicted in Fig. 22.

For the first mode shown in Fig. 22(a), currents on the radiating body and the feeding strip are flowing in the same direction, whereas a current null appears on the feeding strip in the second mode, as shown in Fig. 22(b). The third mode contains a null at the bottom of the radiating body and another on the feeding strip (Fig. 22(c)). For the fourth mode illustrated in Fig. 22(d), there are nulls at the middle of the radiating body and around the junction between the feeding strip and the radiating body. Finally, in Fig. 22(e),

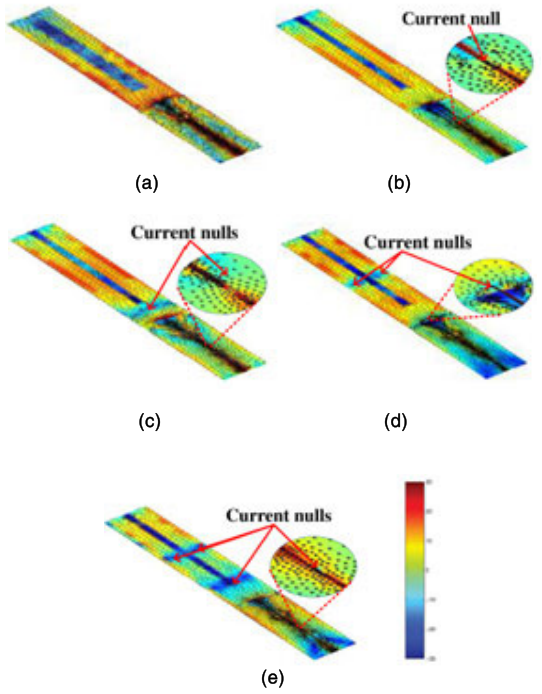

FIGURE 22. Simulated modal current distributions of (a) Mode 1, (b) Mode 2, (c) Mode 3, (d) Mode 4, (e) Mode 5 on the proposed antenna in [27].

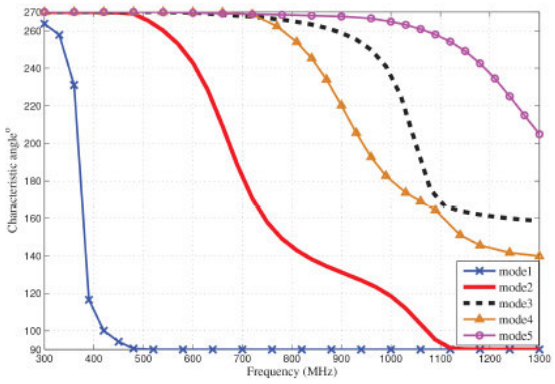

FIGURE 23. Characteristic angles of the five significant modes [27].

two nulls are observed on the radiating body in the fifth mode, and its feeding strip also contain one current null. On the radiating body, all five significant modes have currents located along its length, as expected. Based on this modal surface current analysis, CMA guides designers in selecting the best feeding design and potential methods in its parameter optimization. The antenna operation from 600 MHz to 1 GHz is significantly determined by mode 2. Modes 3 and 4 are dominant within the range of 1 to 1.15 GHz, based on the results of the characteristic angles presented in Fig. 23. The highest resonance is achieved by mode 5.

A U-slot patch antenna is excited separately by using three different probe feeds: a vertical probe, an L-probe, and a T-probe. The resonant behavior produced by using

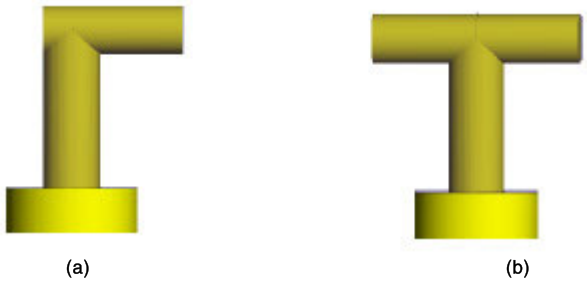

FIGURE 24. Side view of L-probe and T-probe models (a) L-probe (b) T-probe [28].

different feeding probes can be analyzed using CMA. The modal analysis as shown in Fig. 24 concludes that a T-probe feed structure is more resonant and may produce the widest impedance bandwidth [28].

The modal excitation coefficient is analyzed between 2.5 GHz and 8.5 GHz. Modes with the highest modal excitation coefficient values are the main modes excited by the feed probe. Fig. 25(a) shows that mode 3 is the main mode excited by the conventional vertical probe from 2.5 to 5.7 GHz. On the other hand, mode 3 is also the main mode excited by the L-shaped probe between 2.5 and 6.1 GHz, as shown in Fig. 25(b). Finally, in Fig. 25(c), modes 3, 4, and 6 are the main modes excited by the T-shaped probe, from 2.5 to 7 GHz.

Another study in [20] applied CMA to optimize the feeding point for a U-slot microstrip antenna shown in Fig. 26. CMs was first analyzed independent of excitation for the U-slot patch over a frequency band of 2.2 to 2.7 GHz. Without the feeding structure being considered, the CM analyses are only dependent on the shape of the radiating patch. To solve such electrically small problem, the first two CMs are sufficient to describe the resonant behavior of the antenna. All the other modes are assumed as higher order modes which are difficult to excite in practice.'

Fig. 28 shows the current distribution of the proposed antenna, where the vertical mode is subtracted from the horizontal mode. It is observed that the minimum current areas are located at the inner edge of the long arms of the U-slot. This was then determined as the optimal feed area for this antenna instead of the patch center.

C. IMPEDANCE MATCHING OPTIMISATION

This section highlights the use of the CMA technique in optimizing the impedance matching of the antenna and identify the maximum power transfer between the source and its load. Besides that, CMA provides a method in optimizing the impedance bandwidth based on the combination of the dominant modes over the required band. Several studies related to these aspects are presented as follows. The first application of CMA to identify impedance mismatch for a circular patch antenna is proposed in [29], as illustrated in see Fig. 29. This then can be further used to optimize the resonant frequency

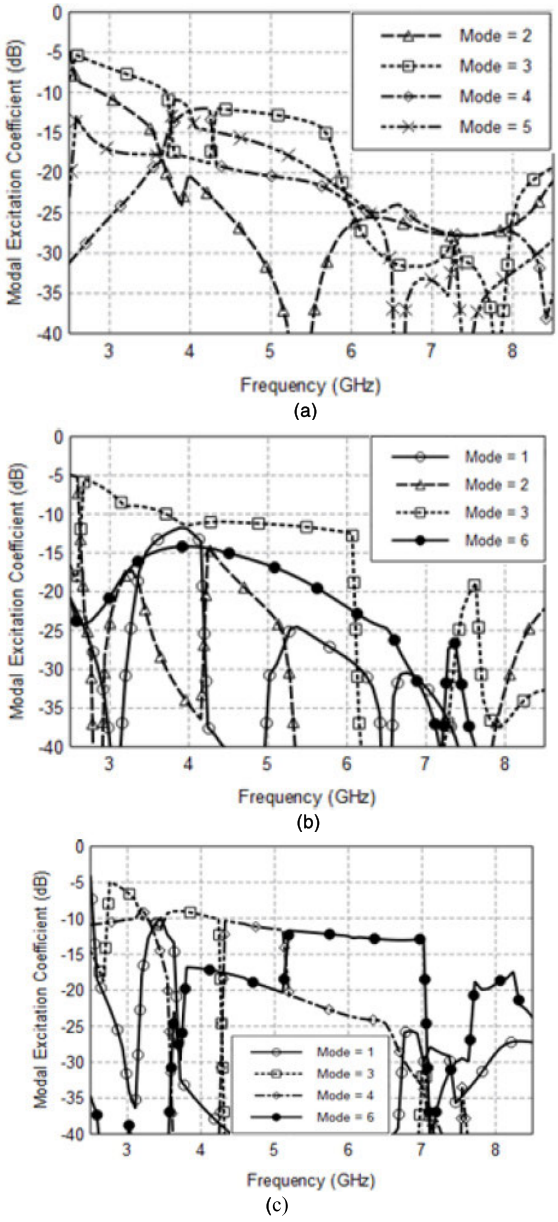

FIGURE 25. Modal Excitation Coefficient of U-slot patch antenna with $\epsilon r = 4.4$ substrate and different excitation feeds. (a) Conventional vertical feed (b) Lprobe feed (c) T-probe feed [28].

and current distributions of the structure. The modal significance of the proposed structure is shown in Fig. 30. It is observed that Modes 1 and 2 have very similar values of modal significance. The superposition of both modal currents is expected to cause impedance mismatch. To alleviate this, the resonant frequency of each mode is separated by inserting slots onto the radiating patch. The effectiveness of this technique is illustrated in Fig. 31. When the resonant frequency of Mode 1 (2.406 MHz) and Mode 2 (1.918 MHz) are separated, it resulted in a resonant bandwidth of 33 MHz (for Mode 1), and 8 MHz (for Mode 2).

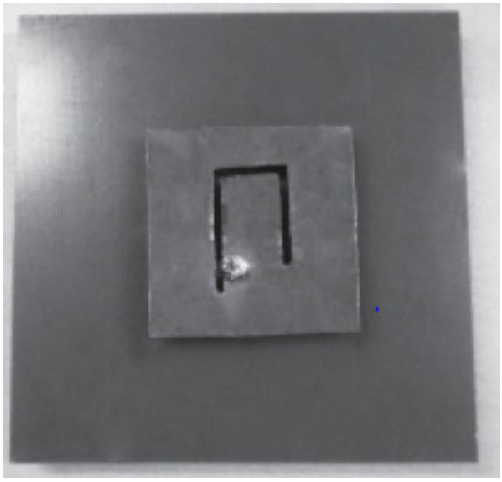

FIGURE 26. Fabricated U-slot antenna [20].

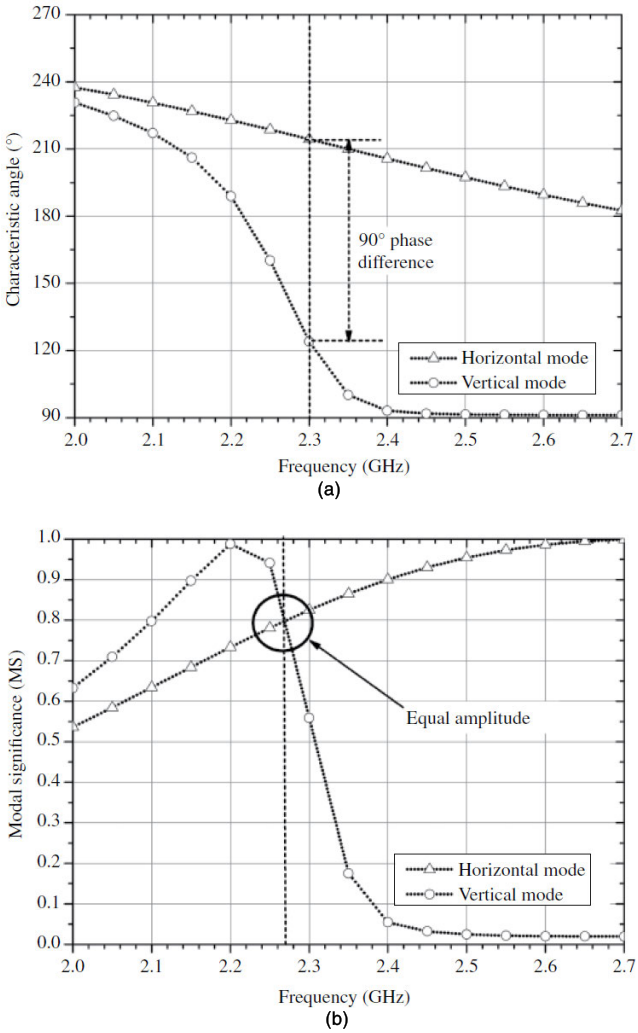

FIGURE 27. CMA results of the U-slot antenna (a): characteristic angle (b): modal significance [20].

Another study designed an ultra-wide band (UWB) antenna operating in the ultra-high frequency (UHF) band using the properties of significant radiating modes. The structure is designed based on a double annular ring with two

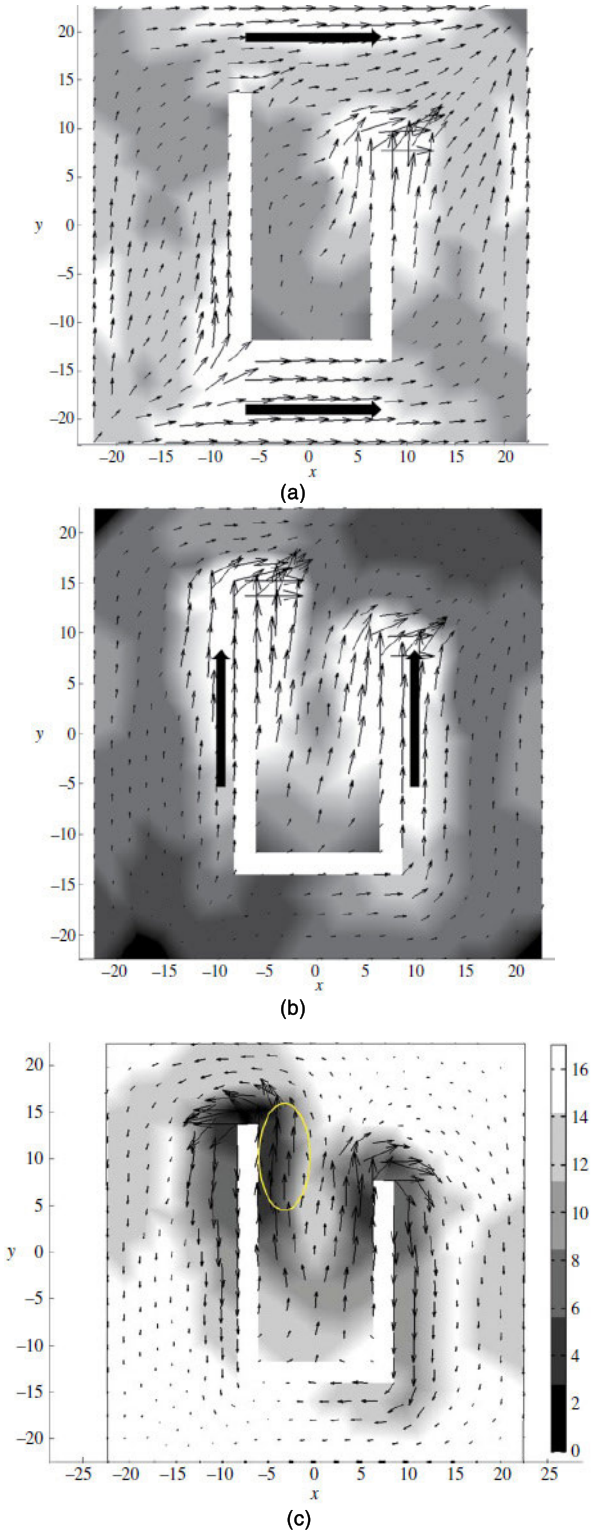

FIGURE 28. Characteristic currents of the U-slot antenna at 2.3 GHz (a): normalized horizontal mode 1 (b): normalized vertical mode 2 (c): H-V current of mode 1 – mode 2. [20].

dipoles, as shown in Fig. 32 [30]. The outer radii of the larger rings are 100 mm × 70 mm, and the smaller ring radii are 48 mm × 30 mm. With the modal properties provided by

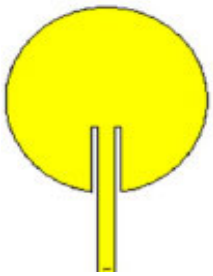

FIGURE 29. Circular patch antenna [29].

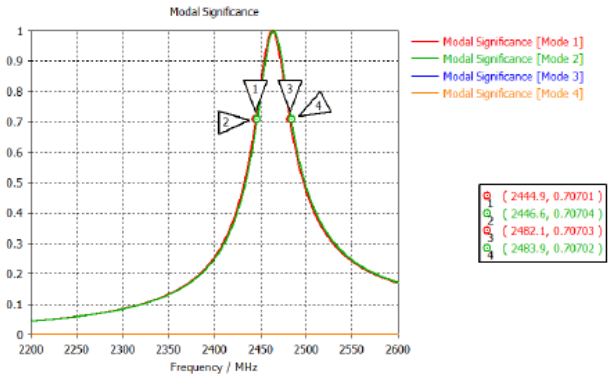

FIGURE 30. Modal significance of PEC circular patch [29].

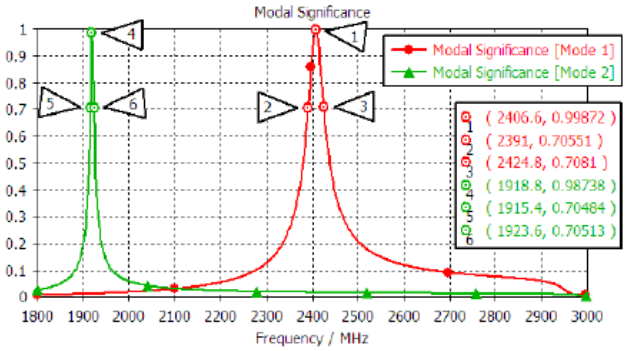

FIGURE 31. Modal significance of the slotted circular patch proposed in [29].

CMA in Fig. 33, the antenna is designed to be excited by energy radiated from dipoles close to it. Therefore, an antenna operating with at least VSWR < 2 from 470 MHz to 960 MHz is achieved by combining the resonances of multiple modes fed through a single port, as shown in Fig. 34.

On the other hand, the work in [31] considered the chassis of the mobile terminal as a part of the radiator. A 50×25 mm^2 conductor sheet is designed with a good radiation behavior to operate in a wideband mode centered at 2.4 GHz. A button is designed as a top loaded monopole antenna and is used to excite the conductive sheet, as depicted in Fig. 35. The design of the main chassis is analysed using CMA to find the proper feed line location. The best position for excitation is determined by observing the location of the current minimum.

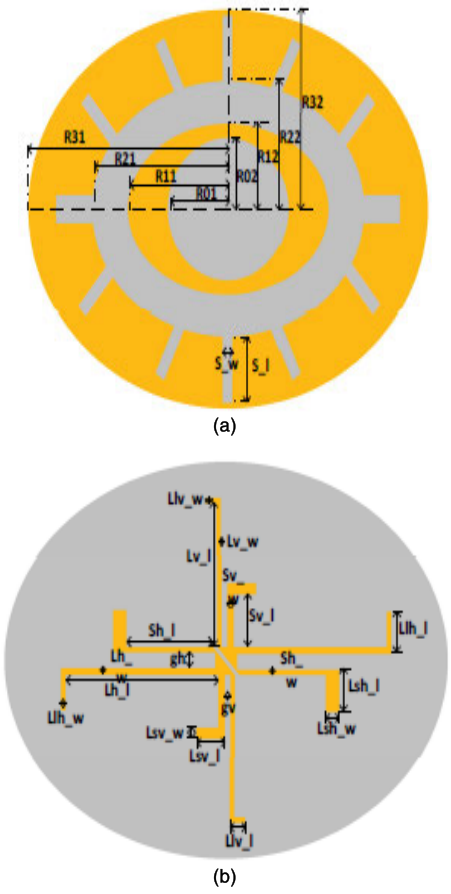

FIGURE 32. Structure of the proposed antenna (a) top view and (b) bottom view [30].

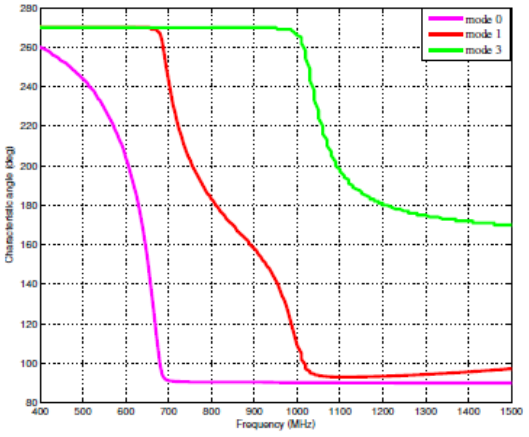

FIGURE 33. Characteristic angle of the double annular ring with two dipoles in different modes [30].

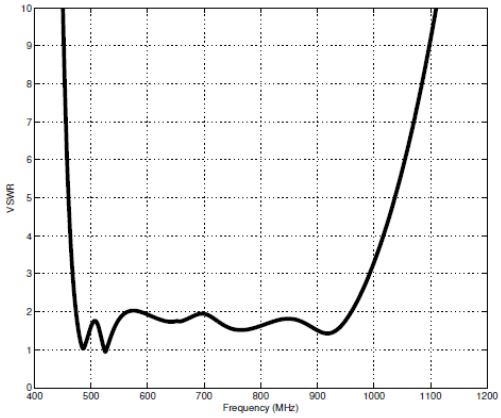

FIGURE 34. Simulated VSWR of the proposed antenna [30].

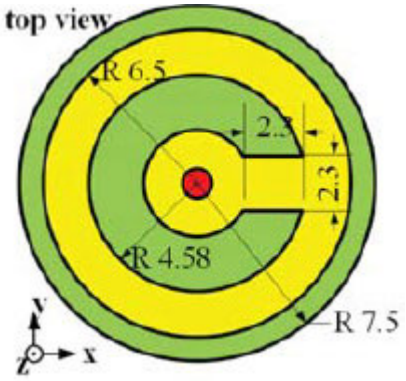

FIGURE 35. Topology of the antenna [31].

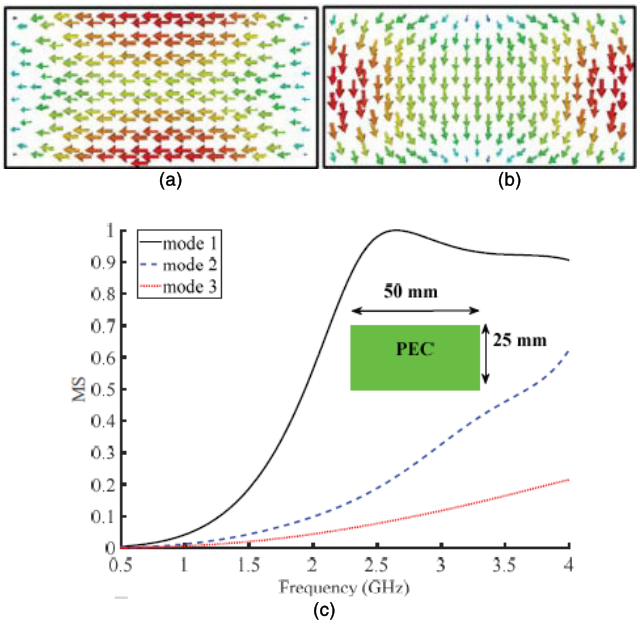

FIGURE 36. Current distribution (a) mode 1 (b) mode 2 (c) MS [31].

The short edge point of the chassis couples with the first mode, as shown in Fig. 36(a) and (b). The modal significance results in Fig. 36(c) shows that the dominant mode resonates around 2.65 GHz.

CMA can also be applied to optimize a nonuniform metasurface array (NMSA) [32]. The proposed NMSA is dimensioned at 27.5 × 7.5 mm^2 and operates in the 5 GHz WLAN band, as illustrated in Fig. 37. The surface currents and radiation patterns for the first six significant characteristic modes from CMA simulations are generated using

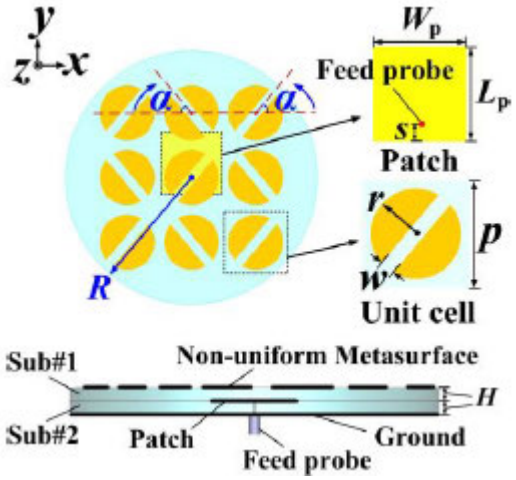

FIGURE 37. Configuration of the proposed NMSA [32].

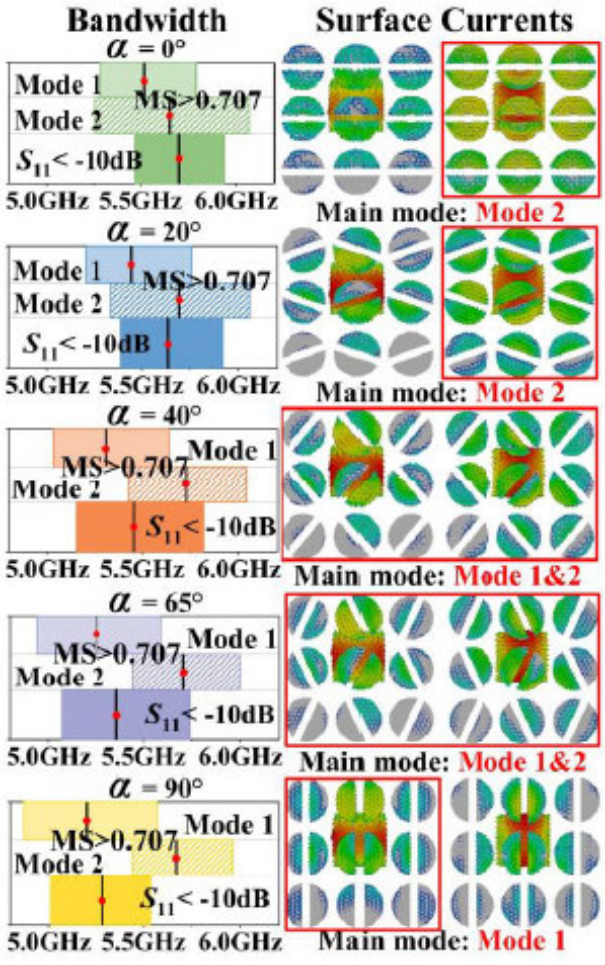

FIGURE 38. Bandwidth and surface current of mode 1 and mode 2 of the nonuniform metasurface antenna [32].

MoM, as shown in Fig. 38. The strength and direction of the currents in each cell of the unit varied, whereas the direction of the combined current distribution is consistent with the patch throughout the entire metasurface. The angular ratio

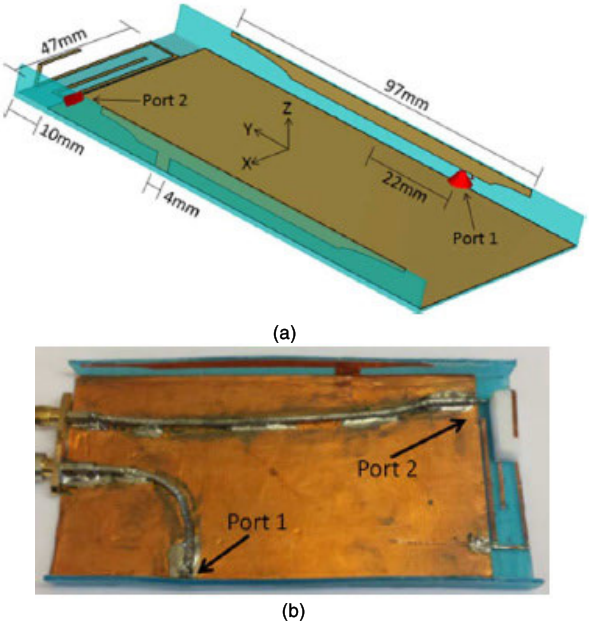

FIGURE 39. The proposed design in [33]: (a) simulated prototype (b) fabricated prototype.

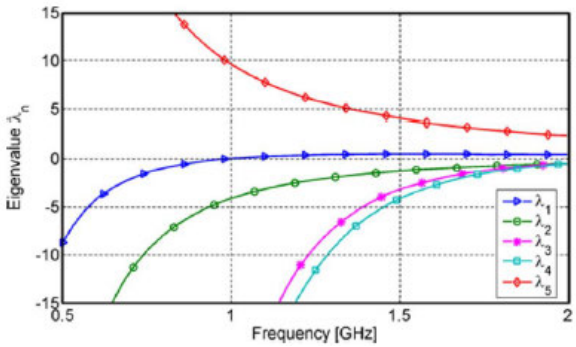

FIGURE 40. Characteristic eigenvalues for the proposed chassis in [33].

is adjusted so that the operation of both dominant modes is combined, resulting in the optimization of its operation throughout the required band.

The study in [33] proposed a new design using CMA to enhance the performance of the orthogonal MIMO antennas. To illustrate the framework, a mobile phone chassis with dimensions 130 × 66 mm^2 as shown in Fig. 39 was analyzed using CMA. The following steps summarizes the work.

i. The first five characteristic modes (λ_1 to λ_5) are tracked by correlating the characteristic currents of each individual mode over frequency and is presented in Fig. 40.
ii. The structure supports only one resonant mode below 1 GHz. This will be referred to as the fundamental chassis mode, which has the same current distribution with a dipole along the length of the chassis, see Fig. 41.
iii. By combining the operation of the characteristic currents and near fields of the significant modes into the frequency band, a single feed can be designed to excite

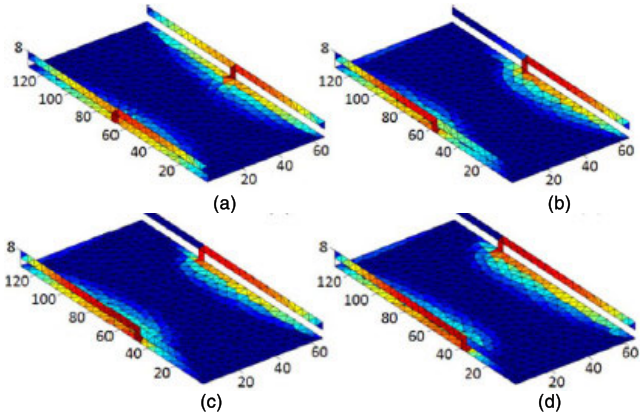

FIGURE 41. Normalized current distribution of λ_1 on the chassis in [33].

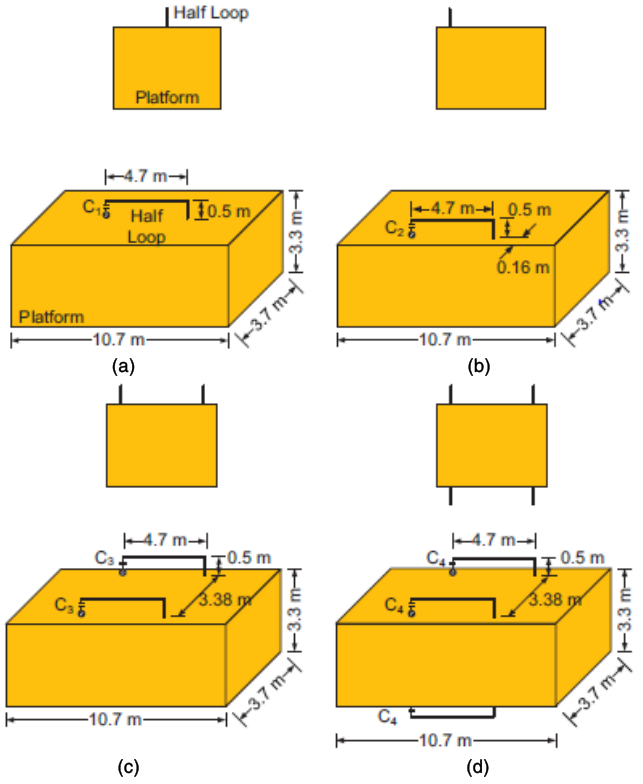

FIGURE 42. (a) A half loop antenna on top of the platform (Center). (b) A half loop antenna on top of the platform (edge). (c) Two half loop antennas on top of the platform (edge). (d) Four half loop antennas on the top and bottom of the platform (Edge) [34].

multiple modes. This leads to bandwidth broadening, resulting in a dual-band antenna operating from 818 to 896 MHz and from 1841 to 2067 MHz.

Next, the work in [34] proposed a method in exciting the characteristic mode of the platform mounted with the antenna to increase its overall bandwidth. Fig. 42 illustrates the half-loop antennas mounted on the modified corners to enable part of the platform as a reflecting plane.

The proposed design process starts by examining the resonant behavior of the platform. Fig. 43 shows that the dominant

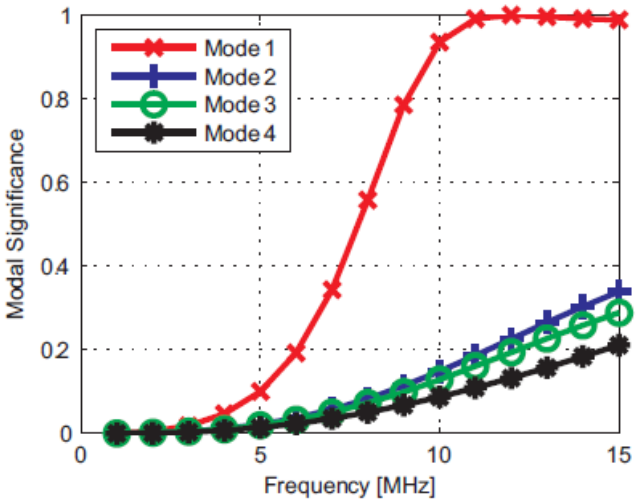

FIGURE 43. Modal significances of the first four modes of the platform [34].

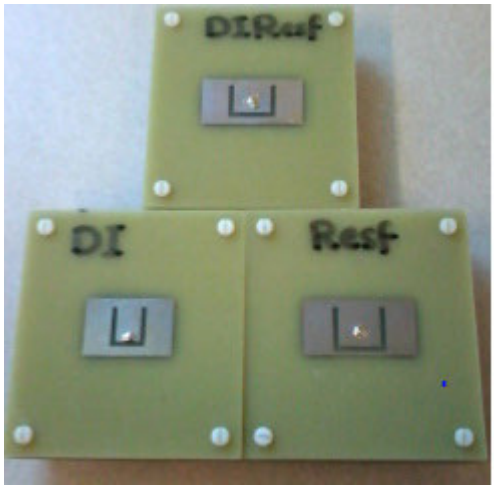

FIGURE 44. Three prototypes of the probe-fed, U-Slot patch antenna [35].

mode for this structure is mode 1, which is significant at approximately 9 MHz.

The desired resonant mode of the platform can then be excited, whereas the bandwidth of the platform-mounted antenna can be enhanced by a factor of 2, 7, or 10 compared to a standalone full loop antenna. This is done by using one, two, or four half loop antennas, respectively, to excite the desired mode. Measured fractional bandwidth of the one, two, and four half loop antennas on the platform are 0.91 %, 1.78 %, and 5.12 %, respectively. Three additional topologies were also evaluated, resulting in a fractional bandwidth of 1.97 % (for three half loop antennas located on the edges and center), 2.84 % (for four half loops located on the edges and center), and 3.75 % (for four half loops antennas located in the center of the platform). This approach provides flexibility in widening bandwidth by increasing the number of loops and by selecting proper locations on the platform.

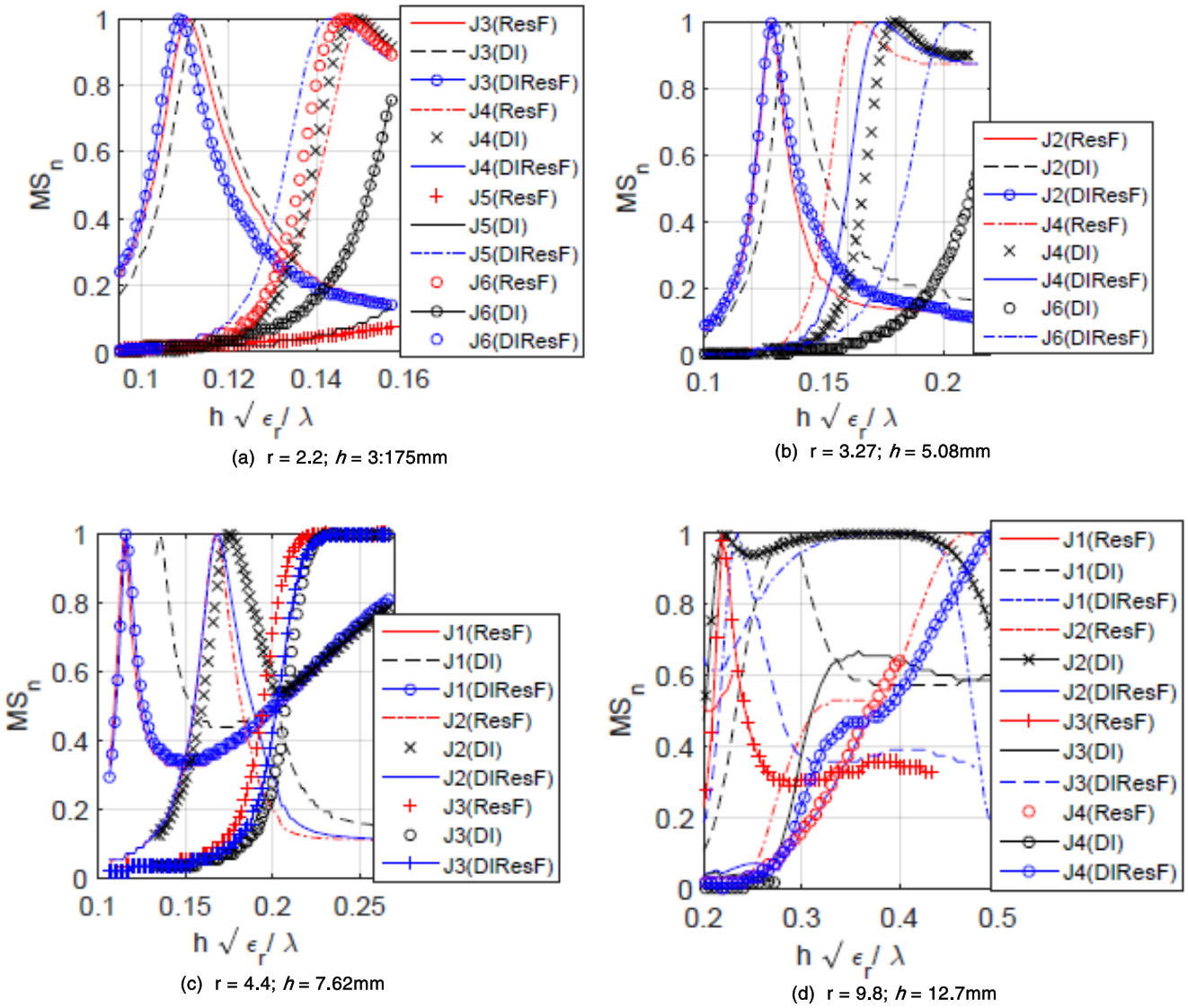

FIGURE 45. Modal characterization of the U-slot antenna for different substrates and dielectric constants [35].

Another study in [35] introduced a method of combining existing design methods i.e., dimensional invariance (*DI*) and resonant frequency (*ResF*) to result in a new empirical design method known as the ''dimensionally invariant resonant frequency (*DIResF*)''. This is aimed at introducing an efficient design process for a wideband antenna, including its feeding probe. As a proof of concept, the design of a probe-fed, U-slot microstrip patch antenna depicted in Fig. 44 is applied on different substrate types and initial thicknesses (t). The proposed methods in this study are descriibed as follows:

i. The empirical *DI* design technique is based on the observation that the dimension of a rectangular patch remains invariant or bears a constant relationship to a symmetrically located U-slot. To obtain the first pass of the design from this method, only the length of the patch, L, is needed, whereas the rest of the patch and U-slot dimensions can be determined from conventional procedures. However, this first pass does not provide for an efficient optimization process of the feeding probes, which potentially affect the resulting surface waves and cross polarization fields.

ii. The second method, *ResF*, is based on the simultaneous excitation of multiple resonant frequencies of a U-slot antenna to result in a broadband response. This design method works well for low permittivity and thin substrates. As ε_r and t increases, the difference between L and the length of the slot, Ls decreases. Similar to the *DI* method, probe location needs to be optimized to obtain an initial U-slot patch design, and this is not straightforward with *ResF*.

iii. The new *DIResF* design method is developed here by combining both design techniques into six steps. This is done to minimize the needed optimization steps of the feed location to obtain optimal bandwidth. By adjusting pre-defined ratios from the *DI* and *ResF* techniques, impedance matching can be controlled with no further

optimization of the feed probe is needed when located at the center of the patch.

The modal analysis of the three design methods (*DI*, *ResF* and *DIResF*) being applied to four different substrates are explained as follows:

i. In case (i), a substrate with $\varepsilon_r = 2.2$ and $t = 3.175$ mm was investigated. Two modes are observed to be simultaneously contributing to the bandwidth when using all three design methods. However, a wider bandwidth is observed for method *DIResF*, as modes 3 and 5 operated at the lower frequencies compared to the other two methods. This increases the fractional bandwidth, as shown in Fig. 45(a).
ii. In case (ii), a substrate with $\varepsilon_r = 3.27$ and $t = 5.08$ mm was investigated. Modes 2 and 4 are seen to operate for all methods except for *DIResF*, where an additional mode 6 is also evident. The current modes in *DI* radiated at higher frequencies than *ResF*, as shown in Fig. 45(b), leading to its higher resonant frequency.
iii. In case (iii), a substrate with $\varepsilon_r = 4.4$ and $t = 7.62$ mm was investigated. Modes 2 and 3 are contributing modes and mode 2 for the *DIResF* technique is excited at a lower frequency. This is almost same as *ResF*, as shown in Fig. 45(c).
iv. Finally, for case (iv), a substrate with $\varepsilon_r = 9.8$ and $t = 12.7$ mm was investigated. Mode 1 and 4 operated for DI, mode 2 and 3 for *ResF*, and mode 1 and 3 for *DIResF*, respectively, to contribute to the total bandwidth, as seen in Fig. 45(d).

D. MIMO

In this section, the CMA approach is utilized as a tool for MIMO antennas' modeling simplification. The specific antenna structural modes and its modal feed network are assessed separately. Each physical mode is assessed by CMA without exciting the antenna. More details of this method and its relevant literature are explained further as follows.

The work presented in [36] proposed a multi-mode multi-element antenna (M^3EA), aimed at realizing multiple uncorrelated antenna ports on each MEA element. This is done by exciting different CMs on the antenna element, as shown in Fig. 46. The base station antenna consists of M rows and N columns of physical elements. As each element is supposed to contain K uncorrelated antenna ports, resulting in $M \times N \times K$ effective antenna ports for the M^3EA.

Fig. 47 illustrates the eigenvalues of the CMs of a rectangular PEC plate as a function of the frequency. This plate is used as a basic antenna element. Within the antenna operating frequency (from 6 GHz and 8.5 GHz), several CMs showed low eigenvalues, which can be effectively excited. The desired modes are excited by direct coupling using sets of gap sources in the open slots. Any modification of the initial structure changes the modal decomposition. Therefore, the modes do not remain the same when the structure is modified from its initial shape.

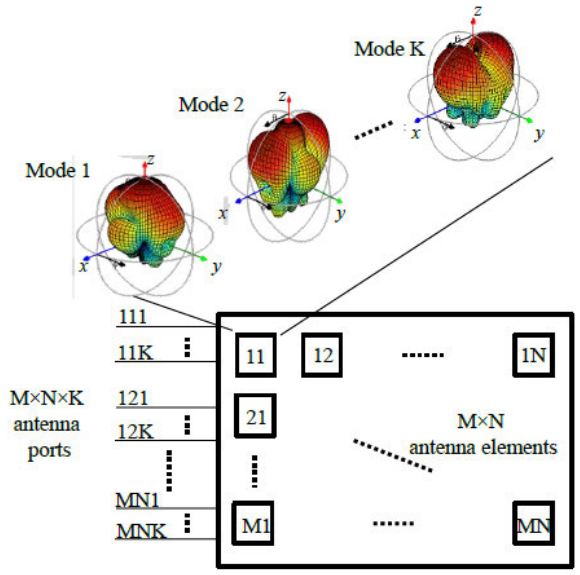

FIGURE 46. Concept of a Multi-Mode Multi Element Antenna (M^3EA) [36].

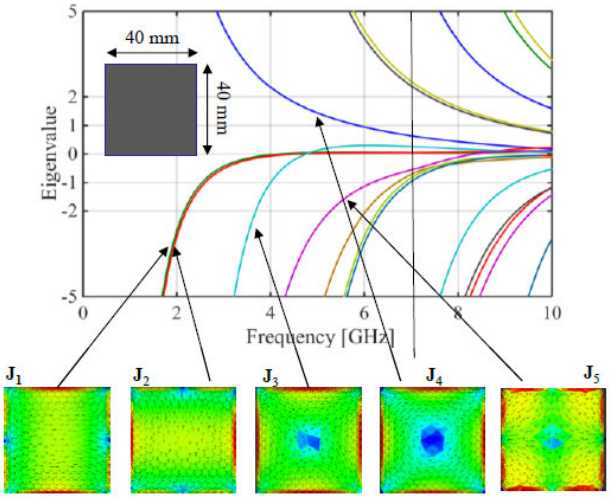

FIGURE 47. Eigenvalues of the characteristic modes of a rectangular plate and modal current density distribution at f = 7.25 GHz [36].

In [37], CMA enables to use of a symmetric conductor as a multiport MIMO antenna using a mode-decoupling network (MDN). The proposed designs are shown in Fig. 48. In the first design step, CMA is performed on the bug-like conductor to find the available set of modes operating within the 2.4 GHz band. Fig. 49 examines the current distribution and radiation pattern for the first three dominant CMs, with a modal significance of 0.98, 0.92, and 0.38 at 2.4 GHz, respectively. Two options are chosen to excite the CMs of the MIMO antenna: one employs ICE, and the other uses capacitive coupling elements (CCE). CCE requires additional components, whereas ICE excitation uses additional slots on the structure. For this reason, ICE has been chosen to be studied. The last two steps involve the excitation of the

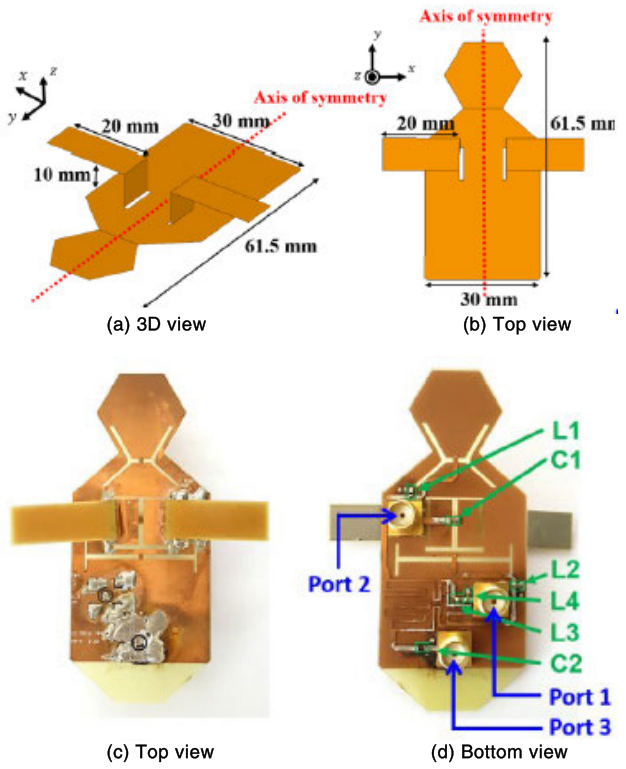

FIGURE 48. Geometry of the biomimetic bug-like structure (a-b): Simulated prototype (c-d): fabricated prototype [37].

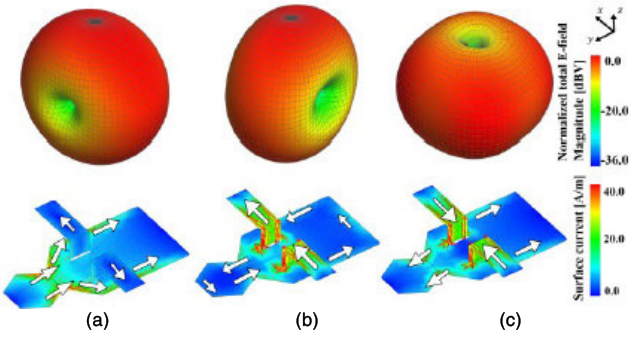

FIGURE 49. Simulated normalized radiation patterns and surface current distributions of the first three dominant CMs at 2.4 GHz (a): Mode 1 (b): mode 2 (c): mode 3 [37].

first three modes and the design of the matching and feeding networks, respectively.

E. SPACE APPLICATIONS

In this section, CMA has been employed to study the antenna parameters for satellite communication. In line with the introduction of more compact pico-satellites, antennas have been designed to provide better space efficiency while maintaining communication system performance. Several studies related to these aspects are presented as follows.

The study in [38] uses the CMA for tailoring a metasurface (MTS) as a superstrate for a compact and low-profile

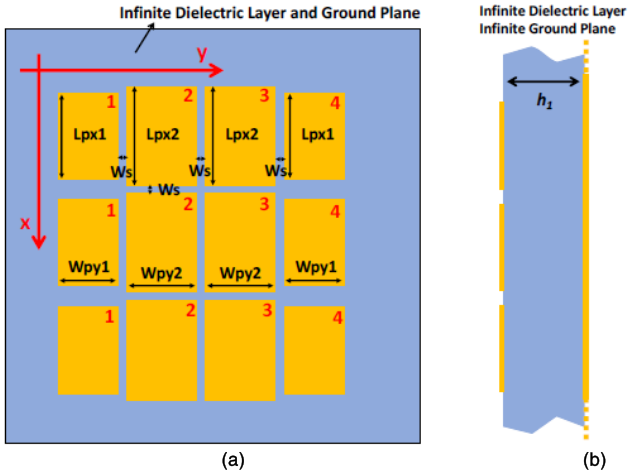

FIGURE 50. (a) Top view and (b) side view of the proposed metasurface superstrate layer with infinite dielectric layer and ground plane [38].

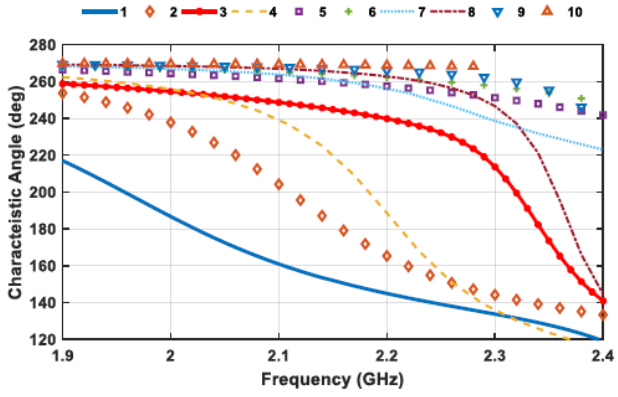

FIGURE 51. The CA of the first ten modes as a function of the frequency [38].

nanosatellite antenna. The final MTS structure consists of non-uniform rectangular patches arranged in a 3 × 4 array configuration, as shown in Fig. 50. The CMA approach is verified by assessing the performance of the overall structure including the stripline feed. To solely account for the effect of 3 × 4 non-uniform upper rectangular patches array, the grounded dielectric layer is considered extended infinitely. The phase difference between the current mode and the related electric field mode, β_n is presented in Fig. 51. It is apparent that at low frequencies, only Mode 1 is near resonance ($\beta_n = 180°$). However, with increasing frequency, more CMs are resonant, contributing to additional radiation if properly excited. The normalized 3D radiation patterns for different CMs are evaluated at 2.15 GHz and illustrated in Fig. 52.

Next, the effects of a finite square ground plane and the introduction of a rectangular slot in Fig. 53 are examined. These modifications shifted the β_n value of Mode 1 down in frequency, whereas the β_n value of Mode 3 slightly rose upwards to 2.2 GHz, relative to the structure with finite ground plane. This is illustrated in Fig. 54.

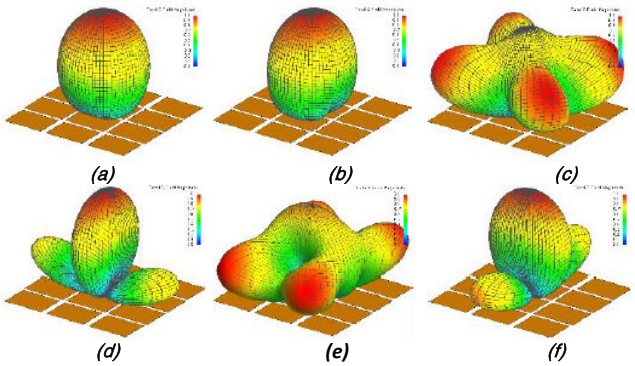

FIGURE 52. Normalized 3D radiation pattern evaluated at 2.15 GHz (a) Mode 1, (b) Mode 3, (c) Mode 6, (d) Mode 8, (e) Mode 9 and (f) Mode 10 [38].

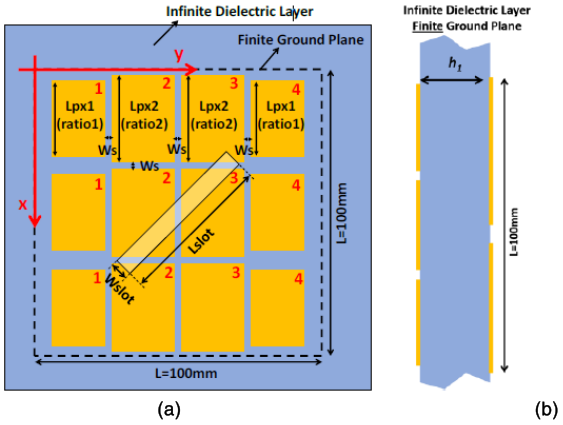

FIGURE 53. (a) Top view and (b) side view of the proposed metasurface superstrate considering the finite ground plane with a rectangular slot. [38].

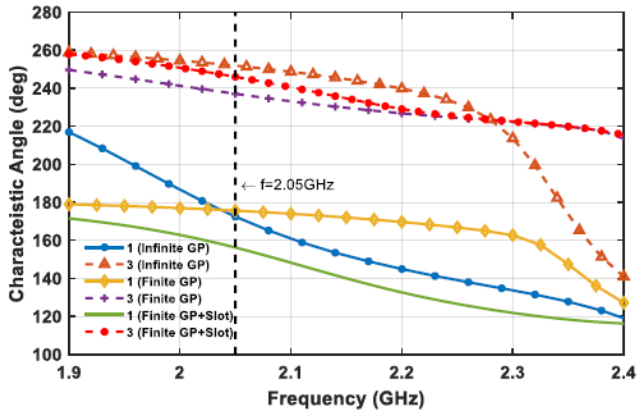

FIGURE 54. Characteristic angle comparison as a function of frequency of the two CMs (Mode 1 and Mode 3) [38].

Next, the study in [39] analyzed a new excitation mechanism called the BIE. It comprises two non-resonant half loops fed with opposite phases and equal magnitude, as seen in Fig. 55(a). Four BIEs are placed at the center of each face edge of the CubeSat, as illustrated in Fig. 55(b). The shape of

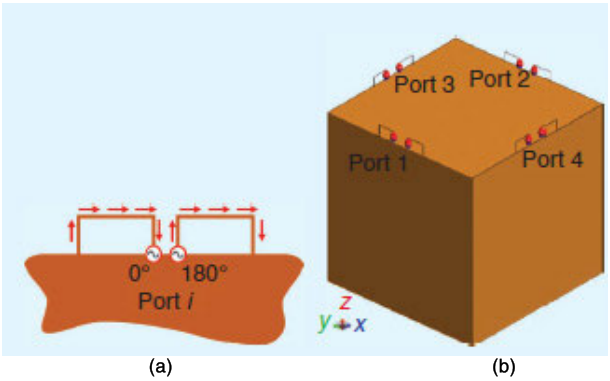

FIGURE 55. (a) A BIE and (b) four BIEs placed on the top CubeSat face. [39].

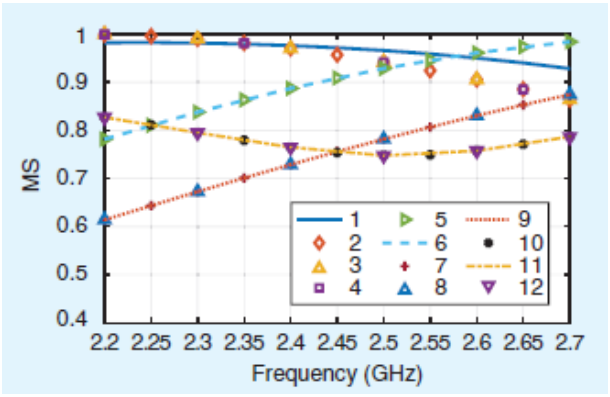

FIGURE 56. MS as a function of the frequency for the first 12 modes [39].

the platform and the BIEs configuration enabled 11 modes to be excited significantly within the 2.4 to 2.45 GHz operating frequency range, as shown in Fig. 56.

Current modes presented in Fig. 57 indicates maxima either located at the center of the edges (modes 1 to 6 and modes 10 to 12) or at the center of a face (modes 7 to 9). The locations of these exciters at the edges are suitable to avoid interfering with solar panels or other platform payloads or systems.

F. METASURFACE

In this section, several important literatures which uses CMA to predict modal behaviors of metasurfaces are presented. Results are then used to analyze and optimize these structures in terms of operating band and radiation characteristics. They are explained in detail as follows.

The study in [40] investigated the metasurface structure as loads (shown in Fig. 58(a)) to improve antenna performance based on CMA. It consists of a single-layered 2 × 2 patch-based metasurface. This research first focused on the pattern configuration before determining the feeding placement. The patch sizes and periods are varied to adjust the resonant frequency of the desired mode, and the calculated modal significance for the first six modes at 35 GHz is presented

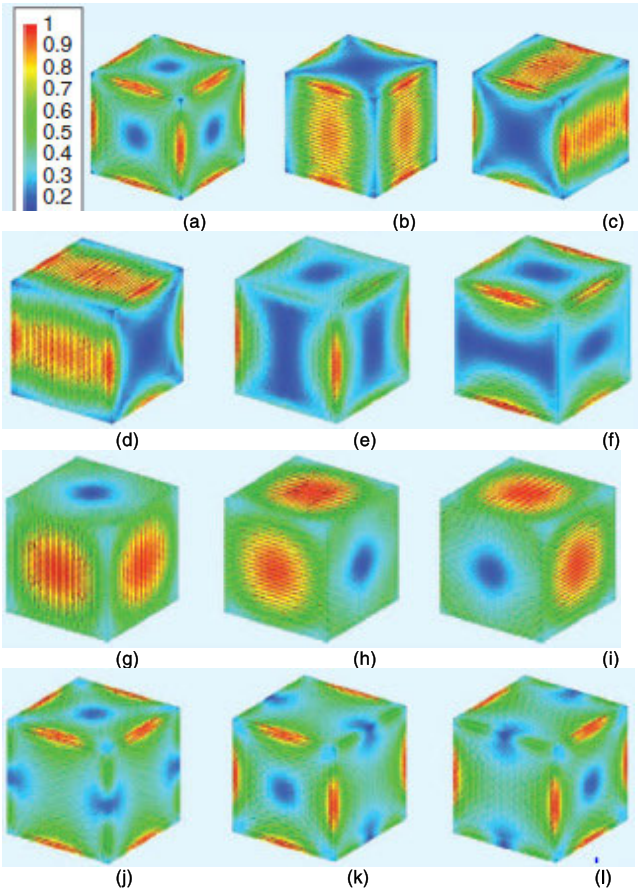

FIGURE 57. The current modes distribution at 2.425 GHz for: (a) mode 1, (b) mode 2, (c) mode 3, (d) mode 4, (e) mode 5, (f) mode 6, (g) mode 7, (h) mode 8, (i) mode 9, (j) mode 10, (k) mode 11, and (l) mode 12 [39].

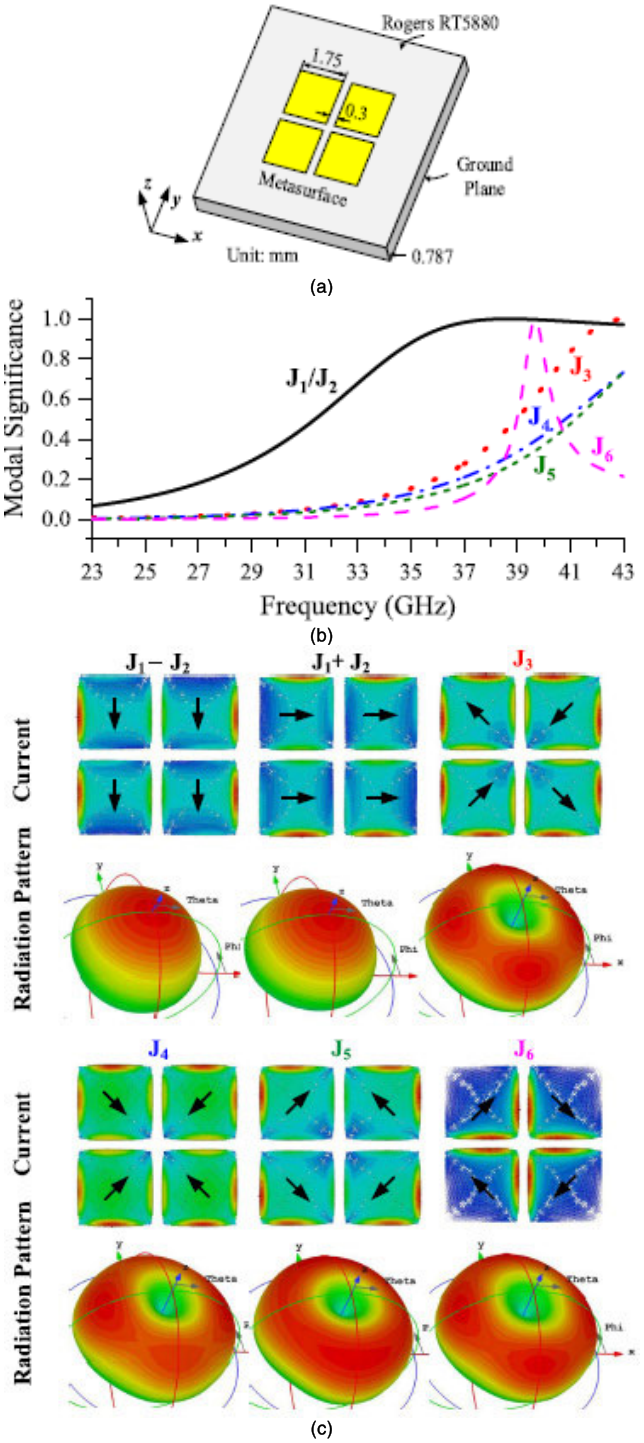

FIGURE 58. CMA of the proposed 2 × 2 patch-based metasurface (a): Configuration (b): Modal significances (c): Characteristic currents and modal radiation patterns of first six modes [40].

in Fig. 58(b). On the other hand, Fig. 58(c) illustrates the characteristic currents and modal radiation patterns of these modes at the resonant frequencies. Else, if the resonant frequencies are beyond the maximum range of 43 GHz, this frequency will be chosen. It is observed that the modes 1 and 2 are a pair of degenerated modes, which combination provides vertically and horizontally polarized radiations at boresight. All the other modes presented are out-of-phase characteristic currents with hollow radiation patterns.

In [41], CMA was used effectively in designing an antenna shown in Fig. 59 by understanding its operating mechanisms and guiding its excitation placement and optimization. The antenna consists of three metallic layers (from top to bottom), a metasurface (P-P' plane), a ground plane (G-G' plane), and a microstrip line (F-F' plane).

The metasurface is located on the top of a 3.454 mm -thick grounded dielectric layer as shown in Fig. 60(a) whereas the first four CMs are shown in Fig. 60(b). As observed, mode 1 and 2 are a pair of resonant modes at 5.9 GHz with the same MSs. Similarly, the other two modes, mode 3 and 4 also resonate and share a similar trend of variation with frequency.

Next, a short slot representing a magnetic current is integrated onto the patch center to selectively excite the desired mode as shown in Fig. 61(a). Due to the small size of the center slot, the characteristic modes are unaffected significantly. However, the first two orthogonal modes start to diverge due to asymmetrical perturbation introduced, as shown in Fig. 61(b).

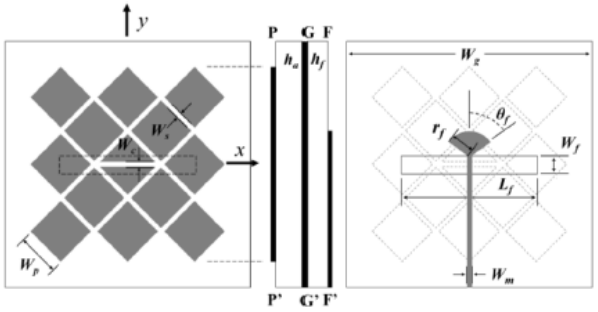

FIGURE 59. Configuration of the proposed antenna [41].

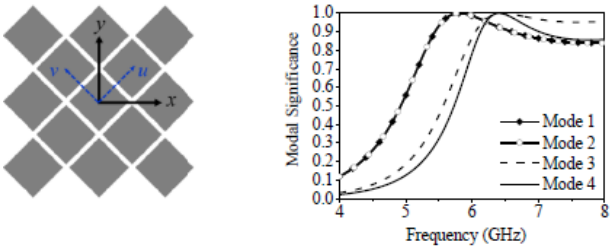

FIGURE 60. (a): Top view of the proposed metasurface which is located on top of an infinite large grounded dielectric layer (b): modal significance [41].

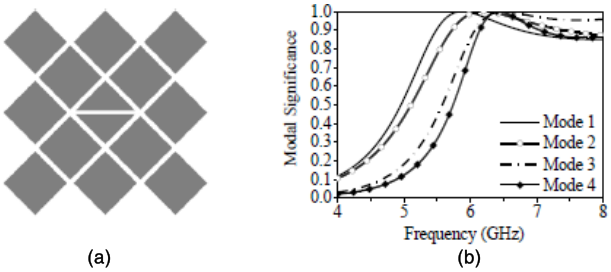

FIGURE 61. (a): Configuration of the metasurface with top slot (b): modal significance [41].

Finally, to further excite the small slot, a long slot representing another magnetic current parallel to the short one is etched on the ground plane, as shown in Fig. 62(a). The MSs of first four characteristic modes for the double-slotted metasurface are plotted in Fig. 62(b). Modes 1, 2, 3 and 4 are resonant at 3.5 GHz, 6.0 GHz, 5.85 GHz, and 6.4 GHz, respectively.

Another study designed a dual-wideband, dual-polarized antenna using metasurface for millimeter-wave (mm-wave) communications using CMA [42]. The proposed metasurface is mainly composed of a 3 × 3 square-patch, as shown in Fig. 63, with four of its corner patches further sub-divided into a 4 × 4 sub-patch array. On the other hand, the size of the other four edge patches is reduced and the center patch is etched with a pair of orthogonal slots.

The design of the metasurface in this study was performed as follows:

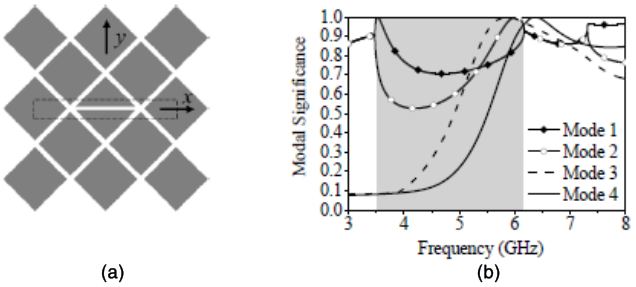

FIGURE 62. (a): Configuration of the metasurface with top and bottom slots (b): modal significance [41].

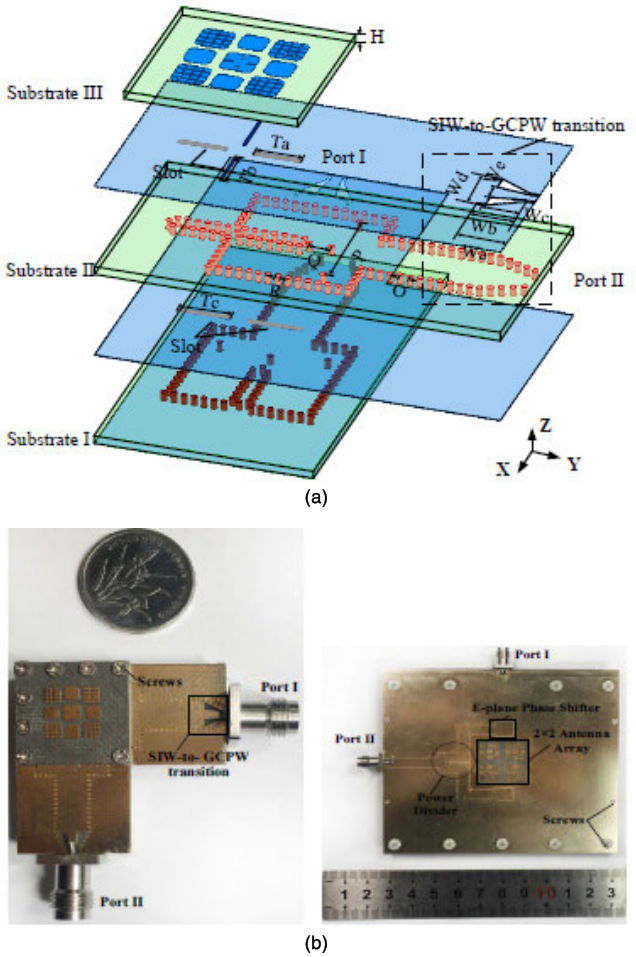

FIGURE 63. Configuration of the antenna element (a): simulated model, (b): fabricated prototype [42].

i. The original metasurface consists of three types of patches: center patch (patch 1), edge patch (patch 2), and corner patch (patch 3), as illustrated in Fig. 64(a).
ii. By etching a quasi-cross slot on patch 1, reducing the size of patch 2, and splitting patch 3 into a 4 × 4 sub-array, an initial modified metasurface with dual-band and suitable radiation patterns is achieved, as depicted in Fig. 64(b).
iii. Next, by moving patch two away from patch 1 (see Fig. 64(c)), the sidelobes of the radiation pattern

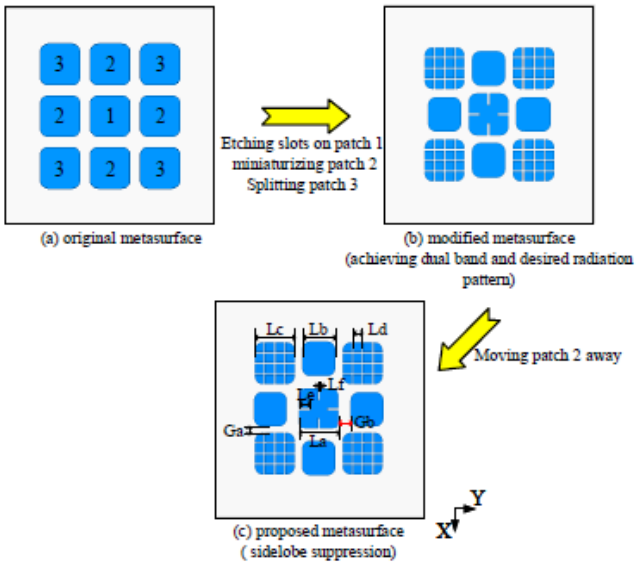

FIGURE 64. Design process of the antenna-element metasurface [42].

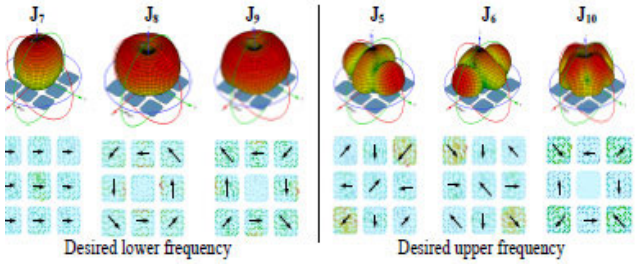

FIGURE 65. Radiation patterns and modal currents of possibly resonant modes for the original metasurface [42].

can be effectively suppressed. Fig. 65 shows the modal radiation patterns of the original metasurface.

To further understand the design process, the following steps depict the operating principle.

i. The original modal significance (MSs) of the first ten modes from 23 to 43 GHz are calculated and sorted at 33 GHz, as shown in Fig. 66.
ii. by etching a quasi-cross slot on patch 1, reducing the size of patch 2, and splitting patch 3 into a 4 × 4 sub-array, a new set of MSs is realized, with its initial modal currents and patterns shown in Figs. 67 and 68, respectively. Only the resonant modes (i.e. mode 1 and 2, mode 4 and 7, and mode 9 and 10) within the desired frequency bands of interest are then selected.

As seen from Fig. 66, the first five modes showed optimal MS magnitudes at 33 GHz (of MS = 1), whereas the rest of the modes (6 to 10) showed magnitudes of greater than 0.707 above 33 GHz, which is acceptable. Due to this, the frequency of 33 GHz is chosen. Moreover, the metasurface structure is modified to achieve dual-band frequencies and the desired radiation patterns by suppressing their sidelobes. On the other hand, Fig. 67 shows that the resonant modes 9

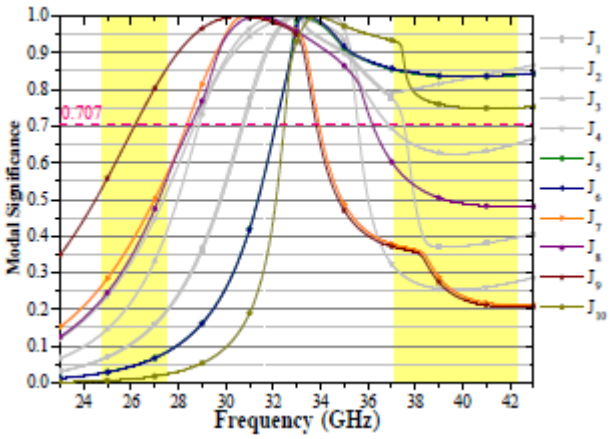

FIGURE 66. MSs of the original metasurface in [42].

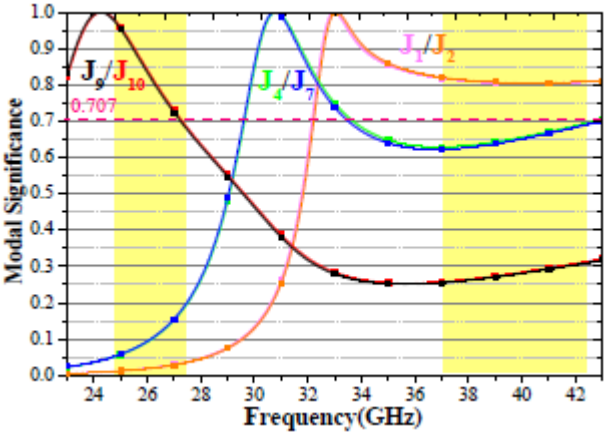

FIGURE 67. MSs of the modified metasurface in [42].

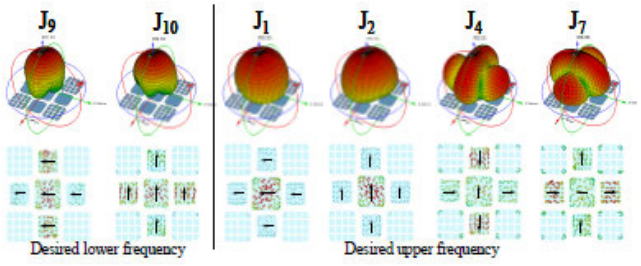

FIGURE 68. Radiation patterns and modal currents of possibly resonant Modes for the modified metasurface [42].

and 10 are excited in the desired lower frequency bands, while resonant modes 1 and 2 are also excited in the desired upper frequency bands. Notice that the modal significance of modes 4 and 7 are close to 0.707, hence they might interfere with the radiations of modes 1 and 2. As a result, a dual band behavior is obtained from the modified metasurface antenna, as indicated by the highlighted areas in Figs. 66 and 67.

Another study in [43] concentrated on improving antenna bandwidth by introducing extra modes from resonant exciters

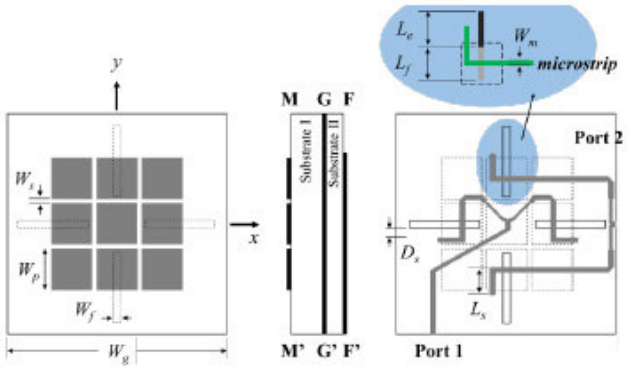

FIGURE 69. Configuration of the metasurface antenna [43].

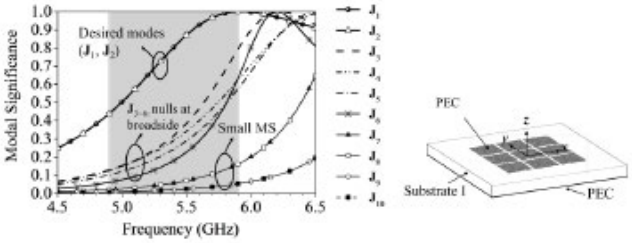

FIGURE 70. Modal significance of the first ten modes of the independent metasurface [43].

in the form of wire (electric currents), aperture (magnetic currents), or both. Resonant metasurface antennas (RMAs) are proposed, as shown in Fig. 69.

A systematic framework is formulated for the design of RMAs using CMA involving resonant apertures. This is done by designing a low-profile wideband dual-polarized RMAs fed by slot arrays at 5 GHz bands. The CMA-based design process of this antenna is explained as follows.

i. The MTS, Substrate I and solid ground are first considered. The MTS is discretized, on which electric currents are solved. Fig. 70 and Fig. 71 show the MS and the characteristic currents for the first ten modes, respectively. Results indicate that the MTS supports two different types of third-order modes (modes 1 and 2) with in-phase currents and broadside radiation patterns.

ii. Secondly, the four resonating slots with Substrates I and II are analyzed separately. The slot areas are discretized by 3328 triangles, in which the Green's function of the planar aperture is defined in FEKO and magnetic currents are solved. Figs. 72(a) and 72(b) show the MS and the associated modal currents for the first four modes, respectively. As can be seen, the four modes present different odd and even symmetries.

iii. As the third step, the dielectric layer for both the slot array and the MTS are considered. Magnetic currents are solved for the slots and electric currents are solved for the MTS, as shown in Fig. 73.

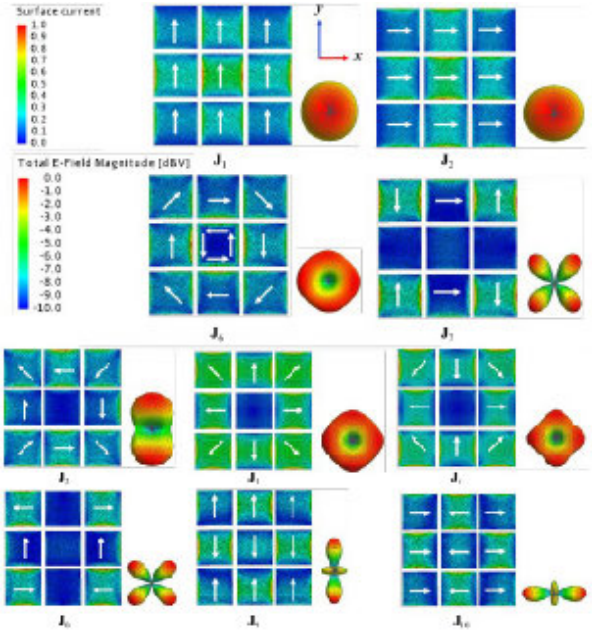

FIGURE 71. Characteristic modal electrical currents and radiation patterns of the first ten modes for the independent metasurface (at 6 GHz) [43].

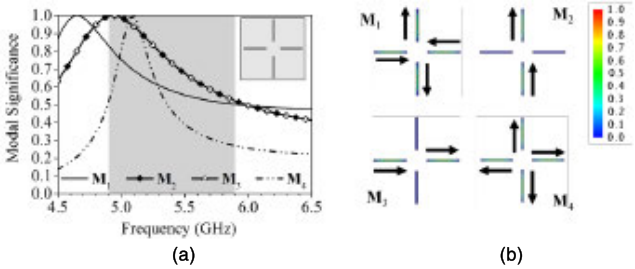

FIGURE 72. (a): Modal significances (b): magnetic currents of the four isolated slots [43].

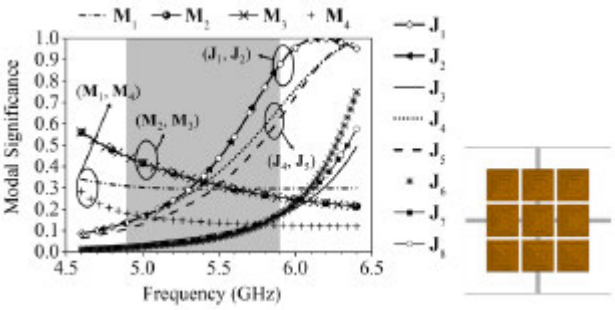

FIGURE 73. Modal significance of the metasurface with four slots [43].

iv. As the fourth step, the purity of mode excitation is evaluated by calculating the far-field radiation power of each mode, as shown in Fig. 74.

G. PLATFORM

In this section, advanced systematic procedures for designing platform-integrated antenna systems using the CMs

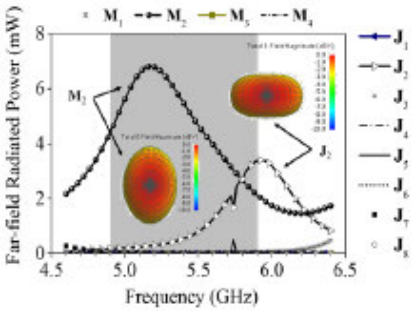

FIGURE 74. Decomposed modal far-field radiating power of 1V voltage excitation [43].

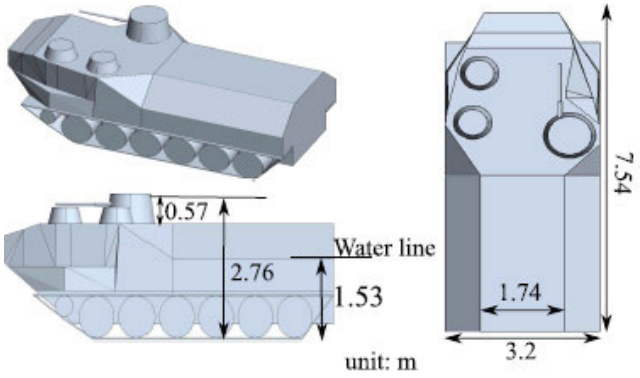

FIGURE 75. AAV model [44].

is presented. The platforms include the likes of naval ships and amphibious assault vehicles and are described as follows.

The study in [44] employed CM theory to adapt the metallic platform as the main radiator. Low-profile coupling elements are mounted on different locations of the amphibious assault vehicle (AAV) platform shown in Fig. 75 to excite two orthogonal, horizontally polarized CMs. The systematic design steps of a dual-polarized, platform-based HF antenna system are characterized experimentally. It is intended for Vertical Incidence Skywave (NVIS) applications operating from 3 to 10 MHz. To develop dual-polarized antennas for this application, horizontally polarized modes should be excited on the platform to create strong radiation towards the zenith.

The CMs of this platform were analyzed in different environments (corresponding to dry and wet earth as well as the seawater). Fig. 76 shows the electric field patterns and normalized surface current distributions of the two horizontally polarized CMs of the AAV at 3 MHz. Mode X (Y) represents the x-polarized (y-polarized) mode with current flowing along the $x(y)$-direction.

Fig. 77 shows the MS values of Modes X and Y from 3 to 10 MHz in these different environments. It is observed that MS values with the presence of dry earth, wet earth, and seawater are larger than those in free space, due to additional conductive ground in the vicinity of the AAV.

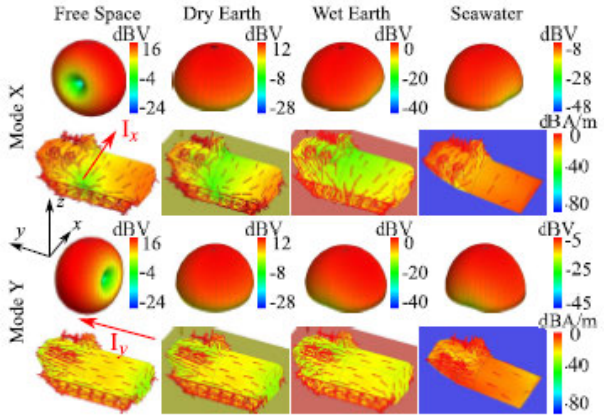

FIGURE 76. Electric field patterns and normalized surface current distributions of the two horizontally polarized CMs (Modes X and Y) of the AAV at 3 MHz [44].

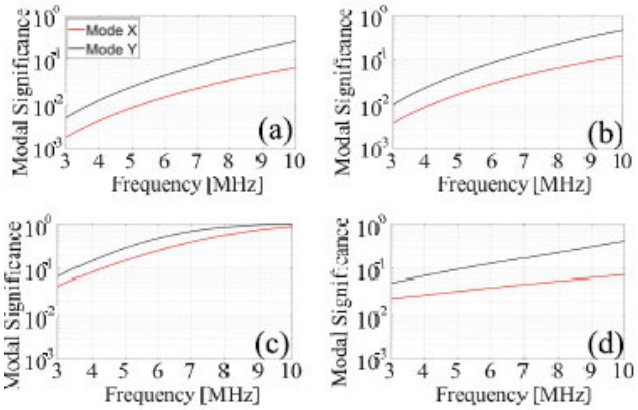

FIGURE 77. MS values of the two horizontally polarized CMs of the AAV from 3 to 10 MHz in different environments (a): Free space (b): Dry earth (c): Wet earth (d): Seawater [44].

Another study in [45] presented an efficient CM-based approach in designing a platform-embedded HF shipboard antenna system. The CMs of the entire ship platform shown in Fig. 78 is calculated to synthesize the desired radiation patterns. Moreover, the localization of the synthesized currents on a small part of the existing platform makes the CM-based structural antenna concept suitable for electrically medium or large platforms.

The CMs are first solved to understand the resonant behavior of the ship platform. The radiating currents are then synthesized to produce the desired radiation patterns using CMs on the ship platform. This is made more efficiently by the modal solutions in CM theory. Thirdly, non-protruding slits are then proposed to excite the synthesized currents. It is seen from Fig. 79 that 20 modes are significant (MS $>$ 0.707) at around 5 MHz. These 20 modes are finally chosen to be synthesized in terms of radiation patterns.

The next study in [46] involves the use of the CMA method for designing an electrically small unmanned aerial vehicle (UAV) antenna system, as shown in Fig. 80. Five steps are

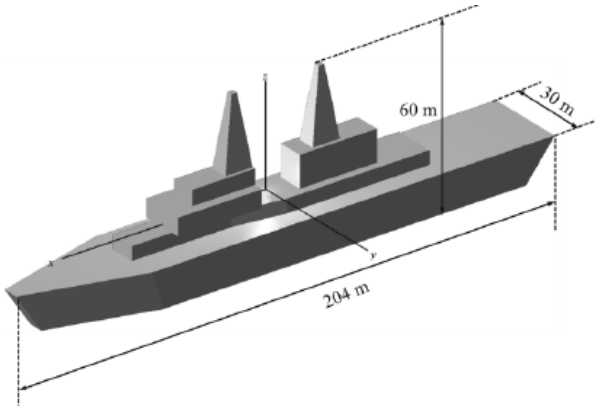

FIGURE 78. Geometry and dimensions of the naval ship [45].

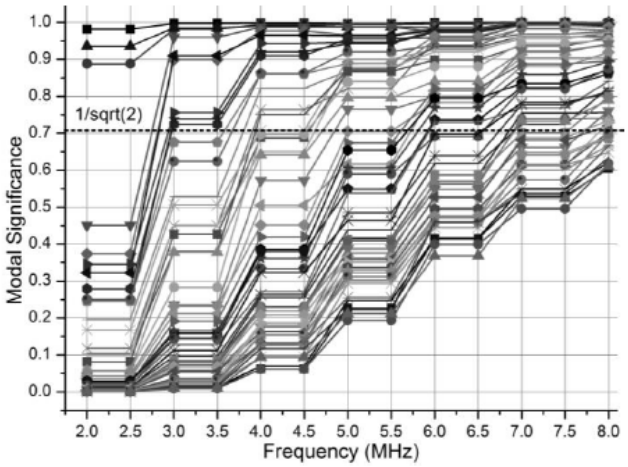

FIGURE 79. Modal significances of the first 50 modes [45].

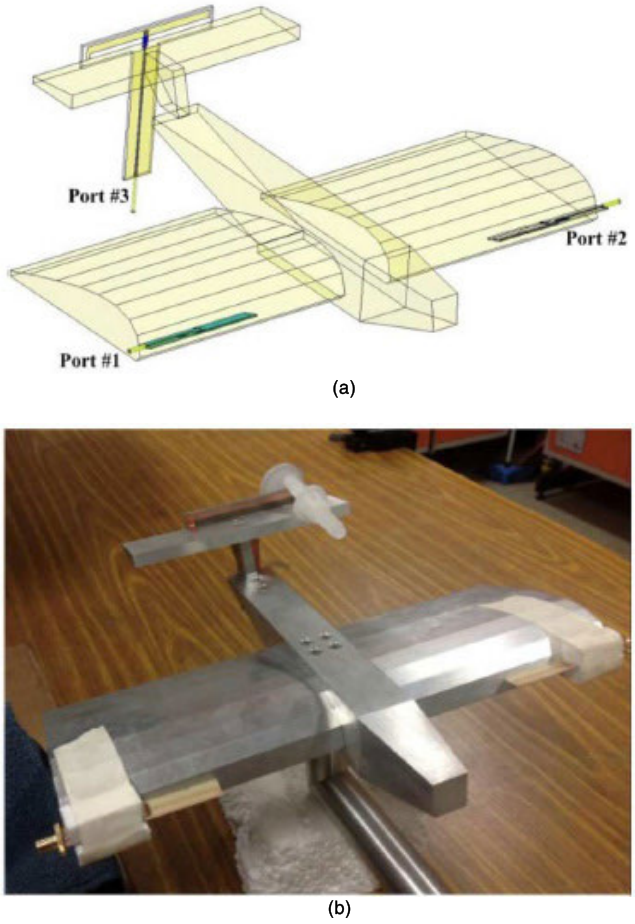

FIGURE 80. Theoretical model (a) and prototype (b) of the three-port UAV integrated antenna system. [46].

involved in applying the CM theory to design this three-port antenna system, as follows:

i. The existing platform which serves as the radiating aperture is integrated with one or more probes, which are used to excite currents on the platform.
ii. The CMs of the platform are applied to synthesize radiation patterns efficiently. The efficiency of the design process is improved by replacing the full-wave simulations with simple linear combinations of CMs.
iii. Small probes are designed to excite the currents for the synthesized radiation patterns. Input impedance matching for each port is also considered.
iv. The overall system is then considered as a single antenna equipped with many ports, capable of producing different radiation patterns by strategized feeding.
v. By scaling the practical HF design problem to the UHF range, a prototype of the designed system is fabricated and measured to validate the presented method.

H. TRACKING OF MODES

Besides being independent of the substrate and excitation, the use of CMA also potentially reduces simulation time in designing antennas, especially for those with large geometries and complex structures. This section focuses on this aim in the design process by tracking CMA modes. More details of the method and its relevant literature is further explained as follows.

When analyzing significant modes in CMA, one important aspect is the ability to track the modes in existence over a target frequency range. It is possible that these modes change order with frequency, or new modes may come into existence and existing modes may vanish with the different frequency [47]. To overcome this, the tracking of modes can be implemented by sorting them according to the order of their eigenvalues [48]. Firstly, the modes are sorted based on the closer to 0 at the lowest frequency (100 MHz). Then, the correlation between the eigen current, J_m at the lowest frequency, and J_n at other frequencies is calculated using equation (6), as follows:

$$\rho_{m,n} = \frac{(J_m)^T J_n}{|J_m|\,|J_n|} \tag{6}$$

Considering the possibility of the weaker modes being insignificant, only the eigen currents with correlation value of over 0.7 are tracked, as shown in Fig 81 [49]. This facilitates

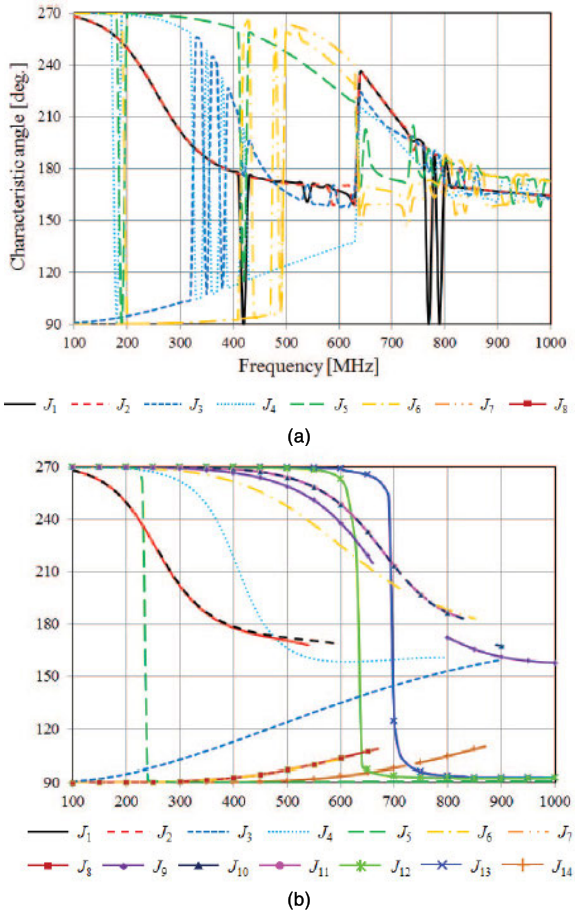

FIGURE 81. Characteristic angle of the antenna (a): without tracking (b): with tracking [49].

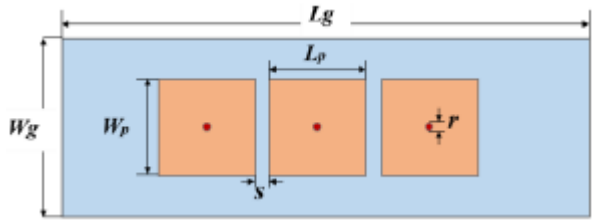

FIGURE 82. End fire antenna structure proposed in [50].

the understanding their behavior, as the different modes may swap order, and significant mode may arise or vanish during the sequential optimization steps. Thus, the structure may be optimized by tracking these modes.

Another study presented a 300 × 100 mm^2 vertically polarized near-end-fire antenna, which is compact in size, high in gain, and features low side lobe levels (SLL) [50]. The proposed antenna array consists of three-square patches, where three shorting pins are vertically placed along the midlines of each one, as seen in Fig. 82. It operates by coupling two distinctive modes in a way that their respective radiations from one end of the antenna are doubled, whereas

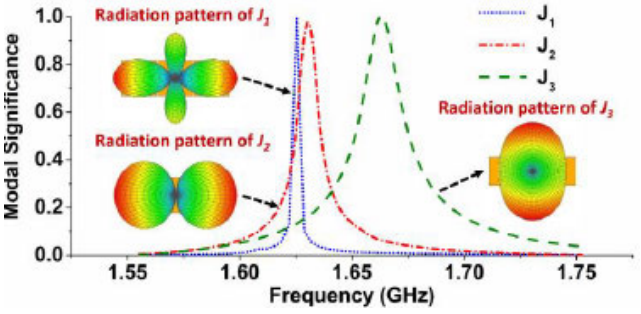

FIGURE 83. Modal significance and radiation pattern of the antenna [50].

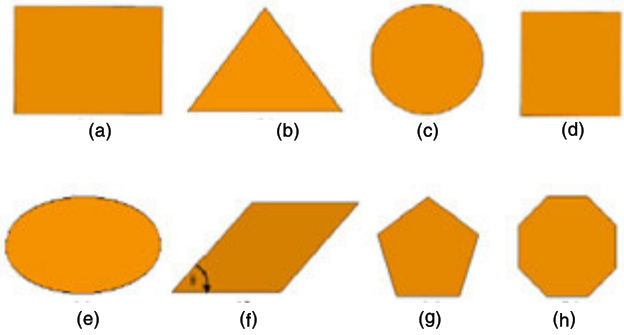

FIGURE 84. Different microstrip patch shapes. (a) Rectangular (b) Equilateral triangular (c) Circular (d) Square (e) Elliptical (f) Parallelogram (g) Regular pentagon (h) Regular octagon [51].

the radiation from the other end are canceled out. In such situation, CMA is an effective tool to identify the resonant modes of an antenna and optimal coupling from perspectives of gain and sidelobe levels. Fig. 83 shows that the first three modes (1, 2 and 3) computed around 1.65 GHz.

The features of CMA can also be applied in analyzing different radiator shapes for a microstrip patch antenna shown in Fig. 84 [51]. This is aimed at choosing the most suitable radiator design by analyzing their resonant behaviors, thus optimizing design and optimization time. Note that these patches are initially analyzed without any substrate, ground, or excitation source to enable the comparison of their resonant behavior. The modal significance is analyzed between 2.5 GHz and 8.5 GHz and is calculated using FEKO software as follows:

i. Modes 1 and 2 are good radiators in the 5.0 to 8.5 GHz range (Fig. 85(a)).
ii. Symmetric modes 1 and 2 are good radiators in the 5.1 to 8.5 GHz range (Fig. 85(b)).
iii. Symmetric modes 1 and 2 are good radiators in the 6.3 to 8.5 GHz range (Fig. 85(c)).
iv. Symmetric modes 1 and 2 are good radiators in the 5.9 to 8.5 GHz range (Fig. 85(d)).
v. Mode 1 is a good radiator in the 4.0 to 8.5 GHz range (Fig. 85(e)).
vi. Modes 1 and 4 are good radiators in the 3.0 to 8.5 GHz range (Fig. 85(f)).

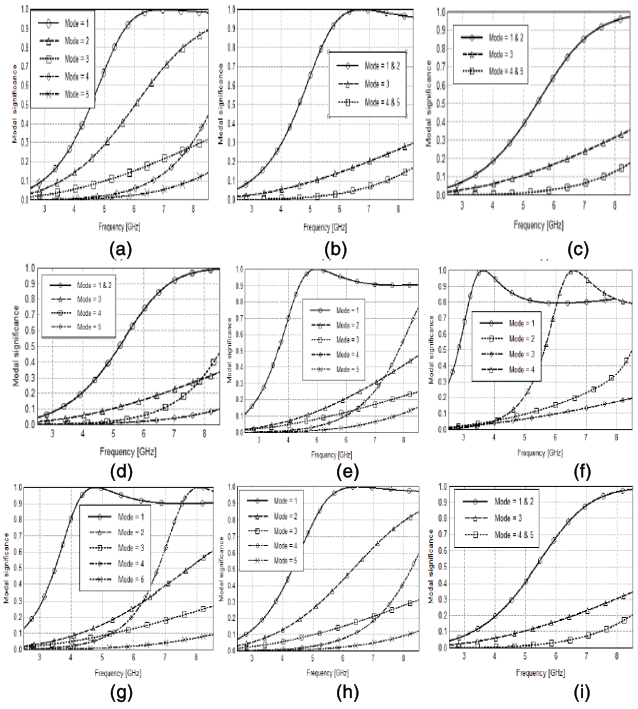

FIGURE 85. Modal significance of different microstrip patch shapes. (a) rectangular (b) equilateral triangular (c) circular (d) square (e) elliptical (f) parallelogram with $\theta = 30°$ (g) parallelogram with $\theta = 44°$ (h) parallelogram with $\theta = 71°$ (i) pentagon [51].

vii. Modes 1 and 4 are good radiators in the 3.8 to 8.5 GHz range (Fig. 85(g)).
viii. Modes 1 and 2 are good radiators in the 4.8 to 8.5 GHz range (Fig. 85(h)).
ix. Symmetric modes 1 and 2 are good radiators in the 6.1 to 8.5 GHz range (Fig. 85(i)).

This study concludes that the parallelogram and elliptical patch shapes are the best radiating structures. Also, the parallelogram patch with the narrowest angle produced the highest modal bandwidth, based on the results presented in Fig. 85.

Another work in [52] applied CMA to design a tunable antenna starting from a ground plane dimensioned at 150 × 70 mm^2. Aimed for operation in the LTE and 5G band, the basic method in this work can be summarized as follows:

i. Firstly, the structure of the chassis is simulated to identify the dominant modes. Simulation results of the chassis shown in Fig. 86(a) indicates that the first mode operates near 800 MHz with a strong surface current density in the center of the chassis (see Fig 87(b)).
ii. Next, an antenna is designed to operate in the lower LTE bands. To do so, the metallic section sized at $L2 =$ 33 mm × $W2 = 35$ mm is removed from one corner of the chassis. The truncated space is then integrated with additional 7-shaped strips, as depicted in Fig. 86(b). This resulted in the surface current concentration near the truncated edge of the chassis, see Fig. 87(d). However, the MS is still maintained around 0.8 GHz, indicating that the modal resonant frequency remained unaffected and its variation is controllable.
iii. The feed position is then slightly displaced away from the location where the strong surface current exists. This shifts the resonant frequency to 1 GHz, making it operational in the lower frequency bands, as illustrated in Fig. 87(a) and (c).
iv. A MIMO antenna is then designed on a 0.762 mm thick RT Duroid substrate ($\varepsilon r = 3.2$, $\tan\delta = 0.0009$), as shown in Fig. 86(c).
v. PIN diodes (denoted as D1 and D2) and varactors (denoted as V1 and V2) in Fig. 86(a) are then

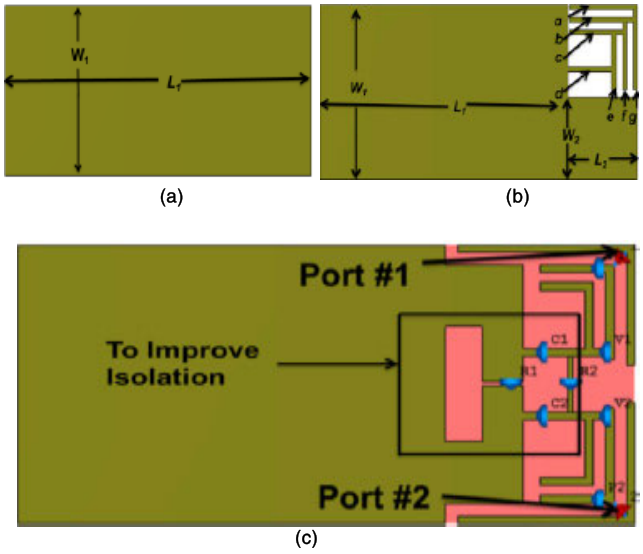

FIGURE 86. Geometry of the antenna proposed in [52], (a) Chassis (b) Truncated chassis (c) MIMO antenna.

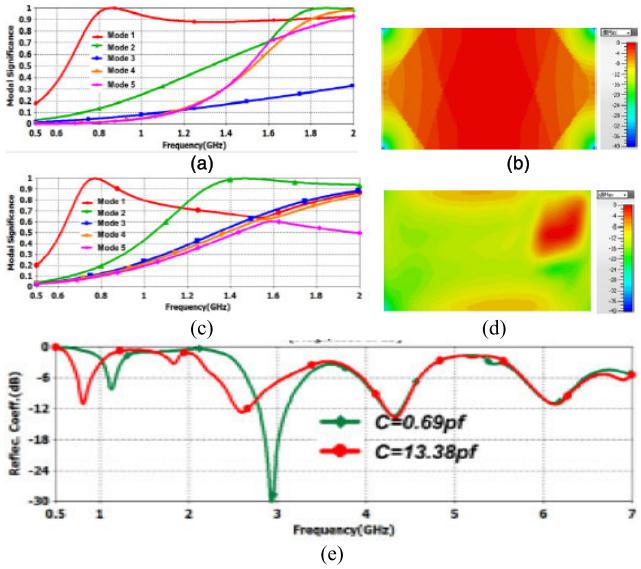

FIGURE 87. (a) MS before chassis truncated (b) characteristic current before chassis truncated (c) MS after chassis truncated (d) characteristic current after chassis truncated (e) Reflection Coefficient Magnitude (dB) [52].

added, introducing simultaneous tunability and switching capabilities.

vi. Finally, a decoupling mechanism to improve the isolation is introduced. The reflection coefficients of the antenna in for the PIN diodes in OFF state is shown in Fig. 87(e). In this state, V1 and V2 are varied from 13.38 pF to 0.69 pF to enable the antenna operation in four bands: from 0.74 to 1.19 GHz, 2.29 to 3.29 GHz, 3.93 to 4.6 GHz, and 5.74 to 6.45 GHz. With a similar variation of V1 and V2 during the ON state of the diodes, the antennas operated from 0.69 to 1.18 GHz and from 5.52 to 6.13 GHz.

V. CONCLUSION AND FUTURE PERSPECTIVES

This paper reviews the recent applications of CMA for different purposes on different antennas. Foreseeing that future antenna designs will be more complex to simultaneously cater to the different wireless standards and stricter constraints, resource-efficient design and optimization procedure for antennas is essential. CMA can be applied in optimizing different antenna performance parameters, as it provides the understanding of the underlying physics of the structure using modes. In comparison with other classical methods, this allows antennas to be designed more systematically and optimized in an efficient way. Antenna dimensions and structures can be modified based on the CMA results, which then provides a good guidance for further adjustment and optimization. It can be summarized that the CMA allows:

i. design of the feed structure based on the desired radiation performance,
ii. attainment of desired radiation patterns by exciting the corresponding modes using feeding location and the eigencurrent distributions,
iii. optimization of impedance matching and identification of the maximum power transfer points between the source and its load,
iv. simplification of modelling MIMO antennas,
v. systematic procedure in exciting the platform and optimizing platform-integrated antennas
vi. optimization of metasurface structures,
vii. tracking and sorting of modes.

It can be summarized that CMA applies to both electrically small and large platforms, providing physical insights into the antenna. This insight aids in choosing the locations of the excitations on the antenna and the antennas on the platform. Moreover, the knowledge of the coupling between excitations and modes enables designers to synthesize the desired antenna, enhancing the impedance bandwidth and forming the radiation pattern. The performance of antennas can be predicted with reasonable accuracy by observing the CMA parameters such as the modal significance, eigenvalue, or characteristic angle. A complete antenna analysis (with substrate and excitation) is then required to fully validate its performance. There are a few main areas that could further advance the use of CMA approach in improving antenna performance. They are listed as follows:

i. Procedure in optimizing the dimensions of planar radiators based on the CMA method for multi-layered substrates with different permittivities.
ii. Development of an analytical model to suppress the unwanted HOMs in the context of compact and large antenna models.
iii. Further quantifying the impact of coupling between the complex probe models of characteristic modes in optimizing an antenna.

Ultimately, overcoming these challenges will make the CMA method more efficient in designing antennas and optimizing their parameters.

REFERENCES

[1] R. Garbacz and R. Turpin, "A generalized expansion for radiated and scattered fields," *IEEE Trans. Antennas Propag.*, vol. AP-19, no. 3, pp. 348–358, May 1971, doi: 10.1109/TAP.1971.1139935.

[2] R. Harrington and J. Mautz, "Theory of characteristic modes for conducting bodies," *IEEE Trans. Antennas Propag.*, vol. AP-19, no. 5, pp. 622–628, Sep. 1971, doi: 10.1109/TAP.1971.1139999.

[3] R. Harrington and J. Mautz, "Computation of characteristic modes for conducting bodies," *IEEE Trans. Antennas Propag.*, vol. AP-19, no. 5, pp. 629–639, Sep. 1971, doi: 10.1109/TAP.1971.1139990.

[4] M. Vogel, G. Gampala, D. Ludick, and C. J. Reddy, "Characteristic mode analysis: Putting physics back into simulation," *IEEE Antennas Propag. Mag.*, vol. 57, no. 2, pp. 307–317, Apr. 2015, doi: 10.1109/MAP.2015.2414670.

[5] A. F. Peterson, S. L. Ray and R. Mittra, *Computational Methods for Electromagnetics*. New York, NY, USA: Wiley, 1997.

[6] E. K. Miller, L. Medgyesi-Mitschang and E. H. Newman, *Computational Electromagnetics: Frequency-Domain Method of Moments*. New York, NY, USA: IEEE Press, 1992.

[7] H. H. Tran, N. Nguyen-Trong, and A. M. Abbosh, "Simple design procedure of a broadband circularly polarized slot monopole antenna assisted by characteristic mode analysis," *IEEE Access*, vol. 6, pp. 78386–78393, 2018, doi: 10.1109/ACCESS.2018.2885015.

[8] M. Ignatenko and D. S. Filipovic, "Application of characteristic mode analysis to HF low profile vehicular antennas," in *Proc. IEEE Antennas Propag. Soc. Int. Symp. (APSURSI)*, Memphis, TN, USA, Jul. 2014, pp. 850–851, doi: 10.1109/APS.2014.6904753.

[9] M. Cabedo-Fabres, E. Antonino-Daviu, A. Valero-Nogueira, and M. Bataller, "The theory of characteristic modes revisited: A contribution to the design of antennas for modern applications," *IEEE Antennas Propag. Mag.*, vol. 49, no. 5, pp. 52–68, Oct. 2007, doi: 10.1109/MAP.2007.4395295.

[10] E. Newman, "Small antenna location synthesis using characteristic modes," *IEEE Trans. Antennas Propag.*, vol. AP-27, no. 4, pp. 530–531, Jul. 1979, doi: 10.1109/TAP.1979.1142116.

[11] H. Kawakami and G. Sato, "Broad-band characteristics of rotationally symmetric antennas and thin wire constructs," *IEEE Trans. Antennas Propag.*, vol. AP-35, no. 1, pp. 26–32, Jan. 1987, doi: 10.1109/TAP.1987.1143967.

[12] K. A. Obeidat, B. D. Raines, and R. G. Rojas, "Antenna design and analysis using characteristic modes," in *Proc. IEEE Antennas Propag. Soc. Int. Symp.*, Honolulu, HI, USA, Jun. 2007, pp. 5993–5996, doi: 10.1109/APS.2007.4396918.

[13] M. Ferrando-Bataller, E. Antonino-Daviu, M. Cabedo-Fabres, and A. Valero-Nogueira, "UWB antenna design based on modal analysis," in *Proc. Eur. Conf. Antennas Propag.*, Berlin, Germany, Mar. 2009, pp. 3530–3534.

[14] E. Antonino-Daviu, M. Fabres, M. Ferrando-Bataller, and V. M. R. Penarrocha, "Modal analysis and design of band-notched UWB planar monopole antennas," *IEEE Trans. Antennas Propag.*, vol. 58, no. 5, pp. 1457–1467, May 2010.

[15] A. Araghi and G. Dadashzadeh, "Oriented design of an antenna for MIMO applications using theory of characteristic modes," *IEEE Antennas Wireless Propag. Lett.*, vol. 11, pp. 1040–1043, Aug. 2012, doi: 10.1109/LAWP.2012.2214198.

[16] A. Krewski, W. L. Schroeder, and K. Solbach, "Multi-band 2-port MIMO LTE antenna design for laptops using characteristic modes," in *Proc. Loughborough Antennas Propag. Conf. (LAPC)*, Loughborough, U.K., Nov. 2012, pp. 1–4, doi: 10.1109/LAPC.2012.6403001.
[17] H. Li, Z. T. Miers, and B. K. Lau, "Design of orthogonal MIMO handset antennas based on characteristic mode manipulation at frequency bands below 1 GHz," *IEEE Trans. Antennas Propag.*, vol. 62, no. 5, pp. 2756–2766, May 2014, doi: 10.1109/TAP.2014.2308530.
[18] P. Miskovsky and A. von Arbin, "Evaluation of MIMO handset antennas with decorative metal elements, using characteristic modes," in *Proc. IEEE Antennas Propag. Soc. Int. Symp. (APSURSI)*, Memphis, TN, USA, Jul. 2014, pp. 1423–1424, doi: 10.1109/APS.2014.6905037.
[19] I. Szini, A. Tatomirescu, and G. Pedersen, "On small terminal MIMO antenna correlation optimization adopting characteristic mode theory," in *Proc. IEEE Antennas Propag. Soc. Int. Symp. (APSURSI)*, Memphis, TN, USA, Jul. 2014, pp. 1425–1426, doi: 10.1109/APS.2014.6905038.
[20] Y. Chen and C.-F. Wang, *Characteristic Modes: Theory and Application to Antenna Engineering*. Hoboken, NJ, USA: Wiley, 2015.
[21] D. Wen, Y. Hao, H. Wang, and H. Zhou, "Design of a wideband antenna with stable omnidirectional radiation pattern using the theory of characteristic modes," *IEEE Trans. Antennas Propag.*, vol. 65, no. 5, pp. 2671–2676, May 2017, doi: 10.1109/TAP.2017.2679767.
[22] X. Yang, Y. Liu, and S.-X. Gong, "Design of a wideband omnidirectional antenna with characteristic mode analysis," *IEEE Antennas Wireless Propag. Lett.*, vol. 17, no. 6, pp. 993–997, Jun. 2018, doi: 10.1109/LAWP.2018.2828883.
[23] F. H. Lin and Z. N. Chen, "A method of suppressing higher order modes for improving radiation performance of metasurface multiport antennas using characteristic mode analysis," *IEEE Trans. Antennas Propag.*, vol. 66, no. 4, pp. 1894–1902, Apr. 2018, doi: 10.1109/TAP.2018.2806401.
[24] F. A. Dicandia, S. Genovesi, and A. Monorchio, "Null-steering antenna design using phase-shifted characteristic modes," *IEEE Trans. Antennas Propag.*, vol. 64, no. 7, pp. 2698–2706, Jul. 2016, doi: 10.1109/TAP.2016.2556700.
[25] F. A. Dicandia, S. Genovesi, and A. Monorchio, "Advantageous exploitation of characteristic modes analysis for the design of 3-D null-scanning antennas," *IEEE Trans. Antennas Propag.*, vol. 65, no. 8, pp. 3924–3934, Aug. 2017, doi: 10.1109/TAP.2017.2716402.
[26] F. A. Dicandia, S. Genovesi, and A. Monorchio, "Efficient excitation of characteristic modes for radiation pattern control by using a novel balanced inductive coupling element," *IEEE Trans. Antennas Propag.*, vol. 66, no. 3, pp. 1102–1113, Mar. 2018, doi: 10.1109/TAP.2018.2790046.
[27] Q. Zhang, Y. Gao, and C. G. Parini, "Compact U-shape ultra-wideband antenna with characteristic mode analysis for TV white space communications," in *Proc. IEEE Int. Symp. Antennas Propag. (APSURSI)*, Fajardo, Puerto Rico, Jun. 2016, pp. 17–18, doi: 10.1109/aps.2016.7695717.
[28] M. M. Elsewe and D. Chatterjee, "Characteristic mode analysis of excitation feed probes in microstrip patch antennas," in *Proc. IEEE Int. Symp. Antennas Propag. (APSURSI)*, Fajardo, Puerto Rico, Jun. 2016, pp. 33–34, doi: 10.1109/APS.2016.7695725.
[29] T. Prakoso, L. Y. Sabila, D. A. Damayanti, A. Sofwan, M. A. Riyadi, Sudjadi, Sukiswo, E. W. Sinuraya, and L. Karnoto, "Bandwidth enhancement of circular microstrip antenna using characteristic mode analysis," in *Proc. 4th Int. Conf. Inf. Technol., Comput., Electr. Eng. (ICITACEE)*, Semarang, IN, USA, Oct. 2017, pp. 312–316, doi: 10.1109/ICITACEE.2017.8257724.
[30] Q. Zhang and Y. Gao, "Design of an UHF UWB doubled annular ring antenna using characteristic mode analysis," in *Proc. 11th Eur. Conf. Antennas Propag. (EUCAP)*, Paris, France, Mar. 2017, pp. 3464–3466, doi: 10.23919/EuCAP.2017.7928719.
[31] S. Yan and G. A. E. Vandenbosch, "Design of wideband wearable antenna using characteristic mode analysis," in *Proc. URSI Asia–Pacific Radio Sci. Conf. (AP-RASC)*, New Delhi, India, Mar. 2019, pp. 1–4, doi: 10.23919/URSIAP-RASC.2019.8738617.
[32] G. Gao, R.-F. Zhang, W.-F. Geng, H.-J. Meng, and B. Hu, "Characteristic mode analysis of a nonuniform metasurface antenna for wearable applications," *IEEE Antennas Wireless Propag. Lett.*, vol. 19, no. 8, pp. 1355–1359, Aug. 2020, doi: 10.1109/LAWP.2020.3001049.
[33] Z. Miers, H. Li, and B. K. Lau, "Design of bandwidth-enhanced and multiband MIMO antennas using characteristic modes," *IEEE Antennas Wireless Propag. Lett.*, vol. 12, pp. 1696–1699, 2013, doi: 10.1109/LAWP.2013.2292562.
[34] T. Shih and N. Behdad, "Bandwidth enhancement of platform-mounted hf antennas using the characteristic mode theory," *IEEE Trans. Antennas Propag.*, vol. 64, no. 7, pp. 2648–2659, Jul. 2016, doi: 10.1109/TAP.2016.2543778.
[35] M. Khan and D. Chatterjee, "Characteristic mode analysis of a class of empirical design techniques for probe-fed, U-slot microstrip patch antennas," *IEEE Trans. Antennas Propag.*, vol. 64, no. 7, pp. 2758–2770, Jul. 2016, doi: 10.1109/TAP.2016.2556705.
[36] D. Manteuffel and R. Martens, "Compact multimode multielement antenna for indoor UWB massive MIMO," *IEEE Trans. Antennas Propag.*, vol. 64, no. 7, pp. 2689–2697, Jul. 2016, doi: 10.1109/TAP.2016.2537388.
[37] D. Kim and S. Nam, "Systematic design of a multiport MIMO antenna with bilateral symmetry based on characteristic mode analysis," *IEEE Trans. Antennas Propag.*, vol. 66, no. 3, pp. 1076–1085, Mar. 2018, doi: 10.1109/TAP.2017.2787607.
[38] F. A. Dicandia and S. Genovesi, "Characteristic modes analysis of non-uniform metasurface superstrate for nanosatellite antenna design," *IEEE Access*, vol. 8, pp. 176050–176061, 2020, doi: 10.1109/ACCESS.2020.3027251.
[39] F. A. Dicandia and S. Genovesi, "A compact CubeSat antenna with beam-steering capability and polarization agility: Characteristic modes theory for breakthrough antenna design," *IEEE Antennas Propag. Mag.*, vol. 62, no. 4, pp. 82–93, Aug. 2020, doi: 10.1109/MAP.2020.2965015.
[40] T. Li and Z. N. Chen, "Wideband sidelobe-level reduced Ka-band metasurface antenna array fed by substrate-integrated gap waveguide using characteristic mode analysis," *IEEE Trans. Antennas Propag.*, vol. 68, no. 3, pp. 1356–1365, Mar. 2020, doi: 10.1109/TAP.2019.2943330.
[41] F. H. Lin and Z. N. Chen, "Low-profile wideband metasurface antennas using characteristic mode analysis," *IEEE Trans. Antennas Propag.*, vol. 65, no. 4, pp. 1706–1713, Apr. 2017, doi: 10.1109/TAP.2017.2671036.
[42] B. Feng, X. He, J. Cheng, and C. Sim, "Dual-wideband dual-polarized metasurface antenna array for the 5G millimeter wave communications based on characteristic mode theory," *IEEE Access*, vol. 8, pp. 21589–21601, 2020, doi: 10.1109/ACCESS.2020.2968964.
[43] F. H. Lin and Z. N. Chen, "Resonant metasurface antennas with resonant apertures: Characteristic mode analysis and dual-polarized broadband low-profile design," *IEEE Trans. Antennas Propag.*, vol. 69, no. 6, pp. 3512–3516, Jun. 2021, doi: 10.1109/TAP.2020.3028246.
[44] K. Ren, M. R. Nikkhah, and N. Behdad, "Design of dual-polarized, platform-based HF antennas using the characteristic mode theory," *IEEE Trans. Antennas Propag.*, vol. 68, no. 7, pp. 5130–5141, Jul. 2020, doi: 10.1109/TAP.2020.2975547.
[45] Y. Chen and C. Wang, "HF band shipboard antenna design using characteristic modes," *IEEE Trans. Antennas Propag.*, vol. 63, no. 3, pp. 1004–1013, Mar. 2015, doi: 10.1109/TAP.2015.2391288.
[46] Y. Chen and C. Wang, "Electrically small UAV antenna design using characteristic modes," *IEEE Trans. Antennas Propag.*, vol. 62, no. 2, pp. 535–545, Feb. 2014, doi: 10.1109/TAP.2013.2289999.
[47] M. Capek, P. Hazdra, P. Hamouz, and J. Eichler, "A method for tracking characteristic numbers and vectors," *Prog. Electromagn. Res. B*, vol. 33, pp. 115–134, 2011.
[48] E. Safin and D. Manteuffel, "Advanced eigenvalue tracking of characteristic modes," *IEEE Trans. Antennas Propag.*, vol. 64, no. 7, pp. 2628–2636, Jul. 2016, doi: 10.1109/TAP.2016.2556698.
[49] M. Yamamoto and H. Arai, "Characteristic modes analysis for patch antenna," in *Proc. IEEE Asia Pacific Microw. Conf. (APMC)*, Kuala Lumpar, Malaysia, Nov. 2017, pp. 1179–1180, doi: 10.1109/APMC.2017.8251668.
[50] Z. Zhang, X. Fu, and S. Cao, "Design of a vertically polarized patch antenna with switchable near-endfire beam using characteristic mode analysis," *IEEE Antennas Wireless Propag. Lett.*, vol. 19, no. 7, pp. 1157–1161, Jul. 2020, doi: 10.1109/LAWP.2020.2992486.
[51] M. M. Elsewe and D. Chatterjee, "Characteristic mode analysis of microstrip patch shapes," in *Proc. IEEE Int. Symp. Antennas Propag. USNC/URSI Nat. Radio Sci. Meeting*, San Diego, CA, USA, Jul. 2017, pp. 2107–2108, doi: 10.1109/APUSNCURSINRSM.2017.8073096.
[52] J. A. Ganie, C. Singh, K. R. Jha, and S. K. Sharma, "A LTE band integrated 5G antenna design using characteristic mode analysis," in *Proc. IEEE Int. Symp. Antennas Propag. USNC-URSI Radio Sci. Meeting*, Atlanta, GA, USA, Jul. 2019, pp. 413–414, doi: 10.1109/APUSNCURSINRSM.2019.8888671.